Lower boundary conditions in Land Surface Models. Effects on the permafrost and the carbon pools.

Ignacio Hermoso de Mendoza[1], Hugo Beltrami[2], Andrew H. MacDougall[2], and Jean-Claude Mareschal[1]

[1]Centre de Recherche sur la dynamique du système Terre (GEOTOP), Université du Québec à Montréal (UQAM), Montréal, Québec, Canada
[2]Climate & Atmospheric Sciences Institute and Department of Earth Sciences, St. Francis Xavier University, Antigonish, Nova Scotia, Canada

Correspondence to: Hugo Beltrami (hugo@stfx.ca)

Abstract.

Earth System Models (ESMs) use bottom boundaries for their land surface model components which are shallower than the depth reached by surface temperature changes in the centennial time scale associated with recent climate change. Shallow bottom boundaries reflect energy to the surface, which along with the lack of geothermal heat flux in current land surface

5 models, alter the surface energy balance and therefore affect some feedback processes between the ground surface and the atmosphere, such as permafrost and soil carbon stability. To evaluate these impacts, we modified the subsurface model in the Community Land Model version 4.5 (CLM4.5) by setting a non-zero crustal heat flux bottom boundary condition and by increasing the depth of the lower boundary by 300 m. The modified and original land models were run during the period 1901-2005 under the historical forcing and between 2005-2300 under two future scenarios of moderate (RCP 4.5) and high

10 (RCP 8.5) emissions. Increasing the thickness of the subsurface by 300 m increases the heat stored in the subsurface by 72 ZJ ($1 \, \text{ZJ} = 10^{21}$ J) by year 2300 for the RCP 4.5 scenario and 201 ZJ for the RCP 8.5 scenario (respective increases of 260% and 217% relative to the shallow model), reduces the loss of near-surface permafrost between 1901 and 2300 by 1.6%-1.9%, and reduces the loss of soil carbon by 1.6%-3.6%. Each increase of $0.02 \, \text{W} \, \text{m}^{-2}$ of the crustal heat flux increases the temperature at the soil-bedrock frontier by 0.4 ± 0.01 K, which decreases near-surface permafrost area slightly (0.3-0.8%), but reduces the

15 loss of soil carbon by as much as 1.1%-5.6% for the two scenarios.

1 Introduction

In the current context of anthropogenic climate change, there is a need to forecast future impacts of climate change as reliably as possible. Future climate change projections are based on simulations from ensembles of Earth System Models (ESMs), numerical models of oceans, atmosphere, land, ice, and biosphere subsystems coupled together (Stocker et al., 2013). Mod-

20 eling of the land system has mainly focused on the interactions between the land surface and the atmosphere (Pitman, 2003), including biogeochemical cycles taking place in the shallow subsurface or soil, such as carbon dynamics (Carmichael, 2008), soil moisture (Seneviratne et al., 2010), vegetation cover and land use (Bonan, 2008), and surface processes such as albedo

and snow cover (Hansen and Nazarenko, 2004). In these Land Surface Models (LSMs) the bedrock layer present below soil is impermeable, and when explicitly modeled, the only process taking place in bedrock is thermal diffusion.

Thermal diffusion in the subsurface allows the land system to act like a heat reservoir, contributing to the thermal inertia of Earth's climate. However, this contribution is relatively small as the capacity of the oceans to absorb energy is orders of

5 magnitude above that of the continents (Stocker et al., 2013). Estimates of the energy accumulation during the second half of the 20th century in the land system show that the heat stored in continents (9 ± 1 ZJ, where 1 ZJ $= 10^{21}$ J) is less than the uncertainty on the heat stored in oceans during the same period (240 ± 19 ZJ) (Beltrami et al., 2002; Levitus et al., 2012; Rhein et al., 2013). This justifies many ESMs to only consider the land subsurface to the shallow depth ($3 - 4$ m) needed for soil modeling (Schmidt et al., 2014; Wu et al., 2014) and neglect the bedrock entirely. Still, the thermal regime of the subsurface

10 affects the energy balance at the surface, which in turn influences the surface and soil processes with a feedback on the climate system. Energy variations at the land surface propagate underground, and the use of a too shallow subsurface in land models implies that these signals are reflected towards the surface, altering its energy balance (Smerdon and Stieglitz, 2006; Stevens et al., 2007).

Several works (MacDougall et al., 2008, 2010) have pointed out that, for the long time scales of climate change, the temper-

15 ature variations at the land surface propagate much deeper than the depths considered in current LSMs, which range between ~ 3.5 m (Schmidt et al., 2014; Wu et al., 2014) and 42 m (Bonan et al., 2013). Theoretical estimates (MacDougall et al., 2008) of heat stored by the subsurface show a difference of one order of magnitude between models using subsurface thicknesses of 10 m and 600 m. This suggests that the reflected energy in shallow land models affects the surface energy balance in the simulations, and current ESMs should use land models sufficiently deep for the length of the simulations, to avoid bottom

20 boundary effects on the thermal profiles.

Most of the current land models use a zero heat flux as thermal boundary condition at their base, as the geothermal gradient is small (~ 0.02 K/m) and does not affect temperature at much shallow depth (Jaupart and Mareschal, 2010). Subsurface models that increase the depth of the bottom boundary to hundreds of meters have to consider the geothermal gradient to properly represent the thermal regime of the subsurface. Such a scheme can be easily implemented by using the Earth's crustal heat flux

25 as bottom boundary condition of the LSM, as a few models already do (Avis et al., 2011).

Soils in permafrost regions act as a long-term carbon sink that stores an estimated 1100-1500 GtC of organic carbon, twice the carbon content of the pre-industrial atmosphere (MacDougall and Beltrami, 2017; Hugelius et al., 2014). The feedback between climate and permafrost thawing and associated carbon emissions is expected to accelerate global warming (Schuur et al., 2015). Rising temperatures at high latitudes induce the thawing of permafrost, leading to the decay of frozen organic

30 matter and the release of CO_2 and CH_4 into the atmosphere. Because of the potential positive feedback of thawing permafrost on the climate system, ESMs endeavor to make robust assessments of future permafrost extent and retreat.

The generation of ESMs used in the fifth phase of the Climate Model Intercomparison Project (CMIP5) show large disagreements in the simulation of present-day permafrost extent. Analyzed across the different LSMs used in CMIP5, the sensitivity of permafrost area to global temperature increase shows a wide range ($0.75 - 2.32 \times 10^6$ km^2 K^{-1}) of sensitivities across the

35 models, and relative permafrost area losses of 6%-29%/K (Slater and Lawrence, 2013; Koven et al., 2013). These differences

arise partly from biases in air temperature and snow depth in some models, but mostly from structural weaknesses of the land models that limit their skill to simulate subsurface processes in cold regions (Koven et al., 2013; Slater and Lawrence, 2013). Most of these land models rely on very shallow (∼3-42 m) subsurface modules (Cuesta-Valero et al., 2016). We expect that, both the thickness of the subsurface and setting a realistic non-zero value of heat flux as bottom boundary condition, will affect

5   the evolution of permafrost in a warming scenario, and therefore the release of permafrost carbon.

It is possible to use analytical methods to estimate the effect that the bottom boundary depth and basal heat flux condition have on the thermal profile of the ground (Stevens et al., 2007). Because of the complexity of the biogeochemical processes in the soil, only numerical simulations can estimate how permafrost dynamics and permafrost carbon content are affected by the changes in the thermal profiles. In this paper, we study the effect of the increase of the lower boundary depth and the addition

10   of a geothermal heat flux at the base of the Community Land Model version 4.5 (CLM4.5) (Bonan et al., 2013), which is the deepest (42.1 m) of the current land models used in the CMIP5 (Stocker et al., 2013). We carried out simulations between 1901 CE and 2300 CE, using historical climate reconstruction between 1901 and 2005 (Viovy, 2011) and explored two alternative scenarios of moderate and high radiative forcings between 2006 and 2300 (Thomson et al., 2011; Riahi et al., 2011).

2   Theoretical analysis

15   The Earth's continental lithosphere (> 100 km) can be considered as a semi-infinite solid for the centennial and millennial time scales considered in the future projection of climate. For a purely-conductive thermal regime of the subsurface, the propagation of a temperature signal at the surface into the ground is governed by the heat diffusion equation in one dimension (Carslaw and Jaeger, 1959):

$$\frac{\partial T}{\partial t} = \kappa \frac{\partial^2 T}{\partial z^2}, \tag{1}$$

20   where κ is thermal diffusivity. The solution of Eq. (1) for a step change T_0 in surface temperature at $t = 0$ yields the temperature anomaly at depth z and at time t:

$$T(z,t) = T_0 \, \mathrm{erfc}\left(\frac{z}{2\sqrt{\kappa t}}\right). \tag{2}$$

The general solution for any surface temperature perturbation $T_0(t)$ starting at $t = 0$ can be obtained as the convolution in time of $T_0(t)$ and the Green function associated to Eq. (1) and the boundary conditions. As the Green function is the solution

25   to a Dirac's delta, it is obtained as the general solution is the time derivative of the solution to the step function in Eq. (2). Therefore, the general solution is:

$$T(z,t) = \frac{z}{2\sqrt{\pi\kappa}} \int_0^t T_0(\xi)(t-\xi)^{-3/2} \exp\left(-\frac{z^2}{4\kappa(t-\xi)}\right) d\xi. \tag{3}$$

Future scenarios (Van Vuuren et al., 2011) predict rising atmospheric temperatures during the present century (Cubasch et al., 2013) with a wide margin of variability and uncertainty. We can represent this future rise in temperatures by a linearly increasing

surface temperature $T_0(t) = mt$, with m being the rate of temperature increase. For such surface temperature function, the solution to Eq. (1) is:

$$T(z,t) = mt \left[\left(1 + \frac{z^2}{2\kappa t}\right) \mathrm{erfc}\left(\frac{z}{2\sqrt{\kappa t}}\right) - \frac{z}{\sqrt{\pi \kappa t}} \exp\left(\frac{-z^2}{4\kappa t}\right) \right]. \tag{4}$$

Numerical models, however, cannot simulate the subsurface as a semi-infinite solid, also known as half space model, but instead limit the subsurface to a given depth, that varies between models. Many land models consider only the upper $3 - 4$ m of the subsurface, which is considered as soil, where hydrological processes take place. Other models further extend the subsurface to include the bedrock below, the deepest currently being the CLM4.5 with a total depth of 42.1 m. We can simplify these models by considering conduction only and modeling the land subsurface as a solid bounded by two parallel planes. Assuming a lower boundary condition of no heat flux (as it is the case in most current models) and a linearly increasing temperature $T_0(t) = mt$ as surface boundary condition, we obtain the following solution (Carslaw and Jaeger, 1959):

$$T(z,t) = m \sum_{n=0}^{\infty} (-1)^n \left\{ \left(t + \frac{(2nd+z)^2}{2\kappa}\right) \mathrm{erfc}\left(\frac{2nd+z}{2\sqrt{\kappa t}}\right) - (2nd+z)\left(\frac{t}{\pi\kappa}\right)^2 \exp\left(-\frac{(2nd+z)^2}{4\kappa t}\right) + \right.$$
$$\left. + \left(t + \frac{(2(n+1)d-z)^2}{2\kappa}\right) \mathrm{erfc}\left(\frac{(2(n+1)d-z)}{2\sqrt{\kappa t}}\right) - (2(n+1)d-z)\left(\frac{t}{\pi\kappa}\right)^2 \exp\left(-\frac{(2(n+1)d-z)^2}{4\kappa t}\right) \right\}, \tag{5}$$

where d is the depth of the bottom boundary. Neglecting near-surface processes such as hydrology or snow isolation, the temperature of the subsurface is described by Eq. (5).

Using Eqs. (4) and (5), we can estimate the effect of the thickness of the model. We have calculated the profiles of temperature perturbation for a rate of surface temperature increase of 0.01 K yr^{-1}, assuming a thermal diffusivity of $\kappa = 1.5\times10^{-6}$ m^2 s^{-1} (used for bedrock in the CLM4.5 (Bonan et al., 2013)). This temperature increase is within the range of global temperature projections for the 21st century (B.Kirtman et al., 2013).
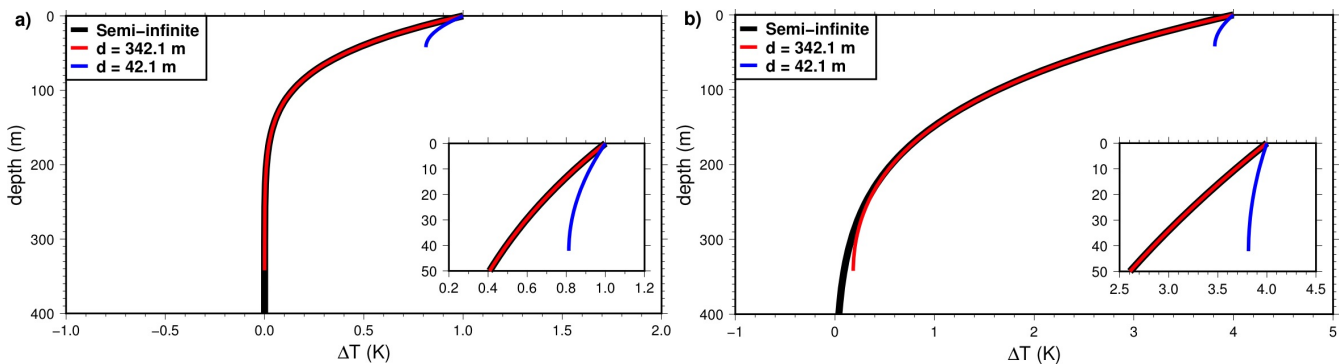

Figure 1. Departure from the initial temperature profile due to constant rate of surface temperature increase of 0.01 K yr^{-1}. Analytical solutions for the half space model (black), and for the finite thickness model with bottom boundary at 42.1 m (blue) and at 342.1 m (red). a) Temperature anomaly after 100 yr. b) Temperature anomaly after 400 yr.

We calculated the temperature anomalies for the half space model and the layers of thickness 42.1 m and 342.1 m, after 100 yr and 400 yr. After 100 yr the temperature anomaly for the thinnest (42.1m) model has departed from that of the half space

Geoscientific
Model Development
Discussions

model (Fig. 1a), while the thickest (342.1 m) model cannot be distinguished from the half space solution after 100 yr. After 400 yr the thickest model only has small departure near the base (Fig. 1b). The response of a model of finite thickness approaches that of the half space model, as long as the bottom boundary is deep enough for the difference between Eqs. (4) and (5) to be negligible.
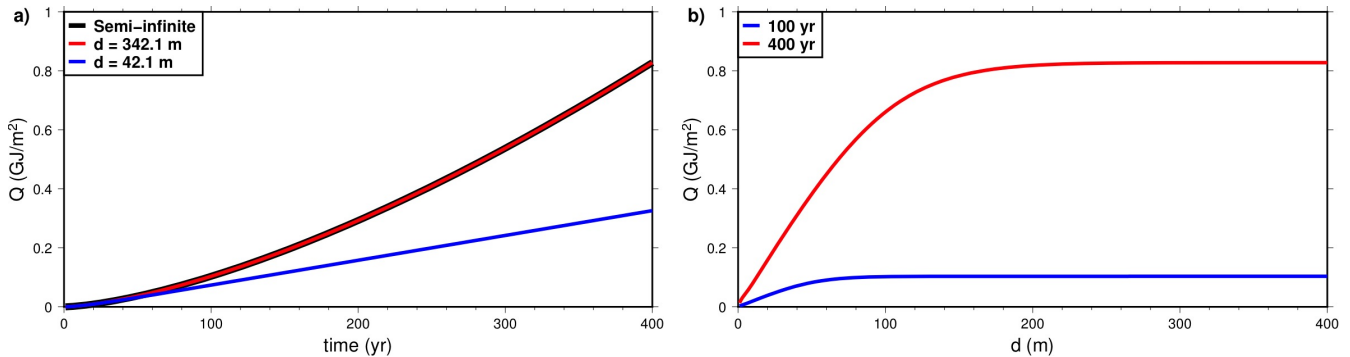

Figure 2. Heat absorbed by the land column per unit of area (Q), following the start of a linear surface temperature increase of 0.01 K yr^{-1}. a): Q as a function of time for the half space model and two models of finite thicknesses 42.1 m and 342.1 m. b): Q as a function of the thickness d of the finite model, at 100 yr and 400 yr.

5   The maximum time before the shallow bottom boundary affects the thermal behavior of the model is better appreciated in terms of heat absorption by the subsurface. The heat stored in the subsurface can be calculated from the temperature change in Eq. (5) by assuming a uniform volumetric heat capacity $c = 2 \times 10^6$ J m^{-3} K^{-1} (taken from bedrock in the CLM4.5).

Figure 2a shows that the heat absorbed per unit of area for the 42.1 m model is slightly smaller than that of the half space model after 100 yr and less than half after 400 yr, while for the 342.1 m model no difference can be observed. Fig. 2b shows
10   how the heat absorbed after 100 yr or 400 yr increases with the thickness of the model, but reaches a plateau where further increase in thickness does not affect heat storage. A bottom boundary depth of 342.1 m is enough for a simulation lasting 400 yr, but a bottom boundary depth of 42.1 m is not adequate for a simulation of 100 yr.

The heat equation (1) shows a scaling relationship between bottom boundary depth d and time t, $d \propto \sqrt{\kappa t}$. This relation can be used as a first order estimate of the depth where the lower boundary does not affect the thermal profiles for a given duration
15   of the simulation and a diffusivity κ. Fig. 2b shows that a bottom boundary depth $d = 100$ m is enough for a simulation of 100 yr, as the heat absorbed by the land column does not increase much with increasing d. A simulation of 400 yr, 4 times longer, needs a bottom boundary depth of $d = 200$ m, only twice as much.

2.1   Geothermal gradient

In the conductive regime described by Eq. (1), the subsurface temperature at a depth z is given as a combination of the
20   geothermal temperature gradient and the temperature perturbation T_t induced by a time-varying temperature signal at the

surface:

$$T(z,t) = T_0 + q_0 \frac{z}{\lambda} + T_t(z,t),$$
(6)

where T_0 is the the mean surface temperature, q_0 is the geothermal heat flux and z/λ is the thermal depth and λ is the thermal conductivity of the subsurface.

5   The propagation into the subsurface of an harmonic temperature signal such as the annual air temperature cycle is characterized by exponential amplitude attenuation $\exp(-\sqrt{\frac{\omega}{2\kappa}}z)$ (Carslaw and Jaeger, 1959), where ω is the frequency of the signal and κ is the thermal diffusivity. At depths of $3-4$ m, the amplitude of the annual signal is several degrees. Given the small values (≈ 0.02 K m^{-1}) of the geothermal temperature gradient in the continents (Jaupart and Mareschal, 2010), the temperature near the surface is dominated by the surface signal T_t. Therefore it may seem reasonable to neglect the geothermal gradient
10   for a thin subsurface layer used in land models (Schmidt et al., 2014; Wu et al., 2014). However, the geothermal temperature gradient can still be influential, even at shallow depths, for temperature-sensitive regimes of subsurface such as permafrost, and it is necessary to determine the lower limit of permafrost. In the case of the CLM4.5 with a subsurface thickness of 42.1 m, the temperature at the bottom of the model is increased by ≈ 0.8 K by a geothermal gradient of 0.02 K m^{-1}. If we were to further increase the thickness of the subsurface, the temperature at the bottom of the model would increase proportionally.

3   Methodology

3.1   Original Land Model

The Community Earth System Model version 1.2 (CESM1.2) is a coupled ESM, consisting of components representing the atmosphere, land, ocean, sea-ice and land-ice. Individual components can be run separately, taking the necessary inputs from prescribed datasets. Because running the coupled model is computationally expensive, we have run only the LSM CLM4.5
20   (Bonan et al., 2013), forced with prescribed atmospheric inputs (Viovy (2011); Thomson et al. (2011); Riahi et al. (2011), see section 3.5.2). These inputs are precipitation, solar radiation, wind speed, surface pressure, surface specific humidity, Surface Air Temperature (SAT) and atmospheric concentrations of aerosols and CO_2.

Carbon and nitrogen cycles are included in the CLM4.5 through the BioGeoChemistry (BGC) module, which includes a methane module (Riley et al., 2011). CLM4.5-BGC can be run at several spatial resolutions. We have used the intermediate
25   resolution $1.89°$lat $\times 2.5°$lon that allows us to compromise between grid fineness and computational requirements. We used the default timestep of 30 minutes (Kluzek, 2013).

The subsurface is discretized in 15 horizontal layers with exponentially deeper node depths:

$$z_i = f_S \left\{ \exp[0.5(i - 0.5)] - 1 \right\},$$
(7)

where $f_S = 0.025$ m is the scaling factor. Layer thickness Δz_i is:

$$\Delta z_i = \begin{cases} 0.5(z_1 + z_2) & i = 1 \\ 0.5(z_{i+1} - z_{i-1}) & i = 2...14 \\ z_{15} - z_{14} & i = 15 \end{cases} \quad (8)$$

The total thickness of the model is 42.1 m. The upper 10 layers, to a depth of 3.8 m, are soil layers where biogeochemistry and hydraulic processes take place. The lower 5 layers are the bedrock, where the only process is thermal diffusion. The soil in each land column has a vertically-uniform clay/sand/silt composition and a vertically-variable carbon density, which determines its thermal and hydraulic properties. Bedrock layers are uniform both horizontal and vertically. The thermal properties for bedrock in CLM4.5, assumed to be made of saturated granite, are a thermal conductivity $\lambda = 3$ W m^{-1} K^{-1} and a volumetric heat capacity $c = 2 \times 10^6$ J m^{-3} K^{-1}, which give a thermal diffusivity $\kappa = \lambda/c = 1.5 \times 10^{-6}$ m^2 s^{-1} (Clauser and Huenges, 1995)).

As the horizontal dimensions of the grid are much larger than the thickness of the subsurface, horizontal heat conduction is considered negligible and thermal diffusion is considered only in the vertical direction as described in Eq. (1). The land subsurface is thermally forced at the surface by its interaction with the atmosphere through latent and sensible heat fluxes, and short and longwave radiation. At the bottom, the model assumes no heat flux.

3.2 Carbon model

The Community Land Model version 4 (CLM4) includes a representation of the carbon and nitrogen cycles (CLM4CN) largely based on the ecosystem process model Biome-BGC (Biome BioGeochemical Cycles) (Running and Hunt, 1993), which is an extension of the previous model Forest-BGC (Running and Gower, 1991). Forest-BGC simulates water, carbon, and nitrogen fluxes in forest ecosystems, which Biome-BGC expanded with more mechanistic descriptions of photosynthesis and by including more vegetation types in its parameterizations. Later versions of Biome-BGC (Thornton et al., 2002) developed the mechanistic calculations of carbon and nitrogen cycles in the soil, control of photosynthesis by nitrogen, differentiation of sunlit/shaded canopies, calculation of fire and harvest, and regrowth dynamics.

In CLM4.5 (Bonan et al., 2013), we work with the BGC carbon model (Riley et al., 2011). The BGC model expands the Carbon-Nitrogen (CN) model by adding a submodel of production, oxidation and emission of methane. CLM4.5 also includes updates to photosynthesis, vegetation and hydrology from CLM4. This improves carbon treatment in CLM4.5-BGC significantly over CLM4CN.

As the schema in Fig. 3 shows, there are three main carbon pools in CLM4.5-BGC: the vegetation, the litter (and coarse wood debris), and the soil organic matter (or soil carbon). These pools are subdivided into several sub-pools. The vegetation has distinct pools to account for the different tissues of the plants: leafs, dead/live stems, live/dead coarse roots, fine roots, and storage pools. Litter and carbon are each defined in the same 10 vertical soil layers used for hydrology, and with 3 separate pools each (corresponding to increasingly recalcitrant forms of carbon) arranged as a converging cascade from coarse wood to litter to soil, a structure known as the Century Soil Carbon pool structure (Bonan et al., 2013).
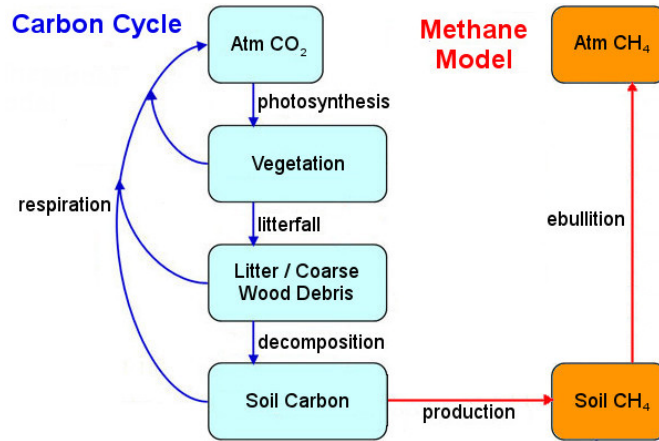
Figure 3. Schema of the carbon flux in CLM4.5-BGC. Figure redrawn from UCAR (2016).

The methane model (Fig. 3) produces CH_4 in the anaerobic fraction of the soil, which consists of the entire soil in the inundated portion of a cell, and the fraction of soil bellow the water table in the non-inundated portion. The CH_4 stays in the inundated soil where is produced for a short time, until it rises to the atmosphere by ebullition. Thus, the production of methane is closely correlated with the hydrology model. In the CLM4.5 hydrology model, the land can store water within the soil (with a thickness of 3.8 m globally, but variable hydrological properties due to its composition) and in an unconfined aquifer with a capacity of 5000 mm globally, implemented as a virtual layer beneath the soil. In reality, soil thickness is highly variable worldwide, in some areas reaching depths of hundreds of meters, while the global mean is estimated at ≈ 13 m (Shangguan et al., 2017).

3.3 Modifications of the original model

We made two main modifications to the LSM. First, we increased the thickness of the bedrock and the depth of the lower boundary. Second, we assumed uniform and constant heat flux as bottom boundary condition. Increasing the thickness of the LSM is necessary to reduce the effect of the lower boundary on the temperature profile. The non-zero heat flux adds the geothermal gradient to the temperature profiles of the subsurface, which allows to determine the lower limit of permafrost in the land column.

We increased the thickness d of the subsurface by progressively adding new layers of constant thickness at the bottom of the land column, to obtain a set of model versions with increasing values of d. The thickness of the added layers must be small to fine tune the depth of the bottom boundary. However, the size of the set is limited by our computational resources, as we aim to increase the depth of the bottom boundary by several hundred meters. As a compromise, we used 12.5 m as the thickness of these new layers. The lowest value of d is 42.1 m (no additional layers, corresponding to the original model) and its highest value is 342.1 m (24 additional layers, with a total thickness of 300 m).

The bottom boundary condition of the LSM is changed to a worldwide uniform value of heat flux. While the continental heat flux is spatially variable, we lack heat flux measurements in wide areas of the world such as South America, Asia and Africa and the Northern Hemisphere permafrost region where heat flux is most important. We use several values of heat flux 0, 0.02, 0.04, 0.06 and 0.08 W m^{-2} to cover the range of heat flow values in stable continents (Jaupart and Mareschal, 2010).

3.4 Permafrost treatment

Near surface permafrost is commonly defined as the permafrost present within the upper 3 m of the soil (Nicolsky et al., 2007; Koven et al., 2011; Schuur et al., 2015), but this depth can be different for some land models where the soil depth is larger than 3 m (Lawrence and Slater, 2005). As in CLM4.5 the soil layers make the upper 3.8 m of the land column, we define near-surface permafrost as the permafrost present above this depth.

Because natural soils can reach deeper than the 3.8 m used in CLM4.5, we aim at gaining some insight on how bottom heat flux and model thickness affect permafrost deeper than 3.8 m. However, it is outside the scope of this study to implement a realistic soil thickness in CLM4.5. For this reason we will also study the permafrost present between the surface and a depth of 42.1 m, the thickness of the thinnest of our model versions, which we define as intermediate-depth permafrost.

While near-surface permafrost and intermediate-depth permafrost define permafrost within a depth range, to study the maximum depth of permafrost we use the concept of Active Layer Thickness (ALT). In environments containing permafrost, the active layer is the upper layer of soil that thaws during summer. The ALT is the maximum depth at which annual temperature variations at the surface are able to thaw the soil, which coincides with the upper limit of permafrost. ALT provides a more complete information on permafrost than the areal extent of soil permafrost, as variations in the thermal regime of the subsurface can displace the upper limit of permafrost in the soil and therefore ALT, but be too small to switch the presence of permafrost within soil.

We are interested in how the modifications to the bottom boundary produce changes in the carbon pools of the permafrost region, but the areal extent of the permafrost region evolves in time. To avoid ambiguities, we define a constant region of study, as the region of the Northern Hemisphere where near-surface permafrost is present at the initial time of the simulations (1901 CE). This region is shown in Fig. 4, and covers parts of North Canada, Alaska, Siberia, Tibet, Inner Scandinavia, and the coast of Greenland. The interior of Greenland, covered by glaciers, is not included in CLM4.5 but it is part of the land-ice model of CESM1.2.

3.5 Simulations

3.5.1 Initialization of the model

We follow the standard spinup procedure (Kluzek, 2013), where the model is initialized with arbitrary pre-initial conditions (no vegetation and uniform subsurface temperature) and driven by a spinup simulation to a steady state (vegetated world adapted to the atmospheric forcings), which can be used as initial condition for the simulation. The spinup period required for the initialization of the model depends on the carbon component used by the LSM. In the case of the CLM4.5-BGC, the
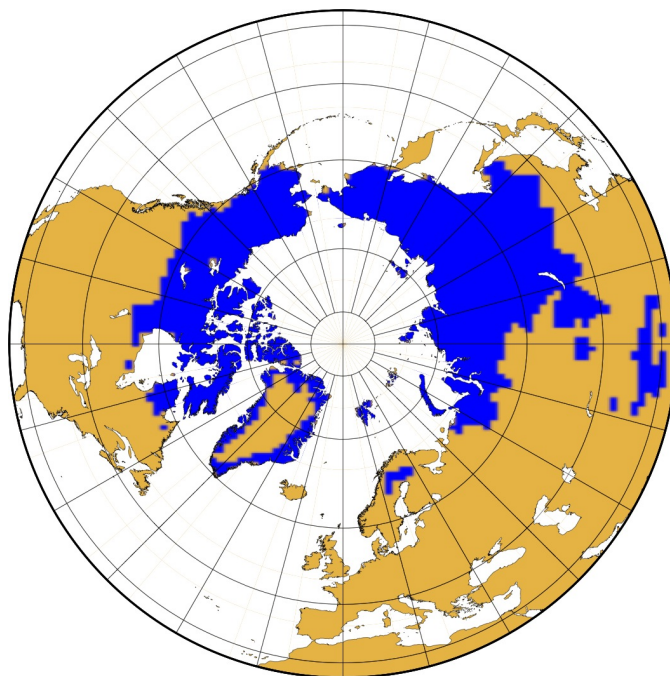
Figure 4. Region of study (blue), which corresponds to the extent of near-surface permafrost in the Northern Hemisphere in the year 1901, for the original CLM4.5 model.

spinup runs 1000 yr with accelerated decomposition rates (which reduces computational costs and performs consistently well (Thornton and Rosenbloom, 2005)) followed by at least 200 yr with normal decomposition rates. During the spinup phase, we use atmospheric forcings (described in section 3.5.2) that correspond to those of the initial years of the simulation, 1901 to 1910.

5   Increasing the depth d of the bottom boundary introduces an additional difficulty to the spinup of the model. In the standard spinup procedure, every soil layer is initialized with a temperature of 274 K independent of the grid cell location, then adapts to the steady state determined by the local surface boundary conditions during the spinup. For a subsurface thickness of $d = 42.1$ m, 1200 yr of spinup are enough for the subsurface to adapt to the steady state. However, the time needed for the subsurface to reach the steady state is proportional to d^2, and 1200 yr is insufficient for the thickest subsurface models. Lengthening the

10   spinup time for each model of increasing thickness d would make computational costs prohibitive.

     To avoid this problem, we only use the standard spinup procedure for the model with the original bottom boundary depth, $d = 42.1$ m. The initial conditions for the models with $d > 42.1$ m are obtained by extrapolating downwards the temperature of the 15th layer with the geothermal gradient of the subsurface. This approach is possible because there are no other variables than temperature in bedrock layers, such as water or carbon content. In addition, as these models depart from a common initial

15   state, we can determine any difference in the final state of these models as dependent from the parameter d exclusively, without the influence of the initial state.

The models with different basal heat flux F_B at the original bottom boundary depth, are individually initialized with the standard spinup procedure. It is not possible to use a common initial condition for these models, because the thermal steady state is dependent on F_B.

3.5.2 Simulation of the 1901-2300 period

5 Each version of the LSM is run offline between 1901 CE and 2300 CE, taking prescribed atmospheric variables from external sources as input to force the model. These simulations include two phases depending on the input used, (1) between 1901-2005, from reanalysis of historical data, and (2) between 2006-2300, from the IPCC climate projection under two warming scenarios (Thomson et al., 2011; Riahi et al., 2011).

The first phase is a historical 20th century simulation between 1901-2005. The forcing data are taken from the CRUNCEP
10 dataset (Viovy, 2011), combination of the Climate Research Unit Time-Series (CRU-TS) monthly climatology (Harris et al., 2014) and the National Centers for Environmental Prediction (NCEP) reanalysis (Kalnay et al., 1996) between the years 1901 and 2005.

The second phase continues the first phase between 2006-2300, forcing the LSM with the atmospheric output from a simulation for a specific trajectory of greenhouse gas concentration. These trajectories, called Representative Concentration Pathways
15 (RCPs), are scenarios of future human emissions and provide a basis to the climate research community for modeling experiments in the long and short terms (Van Vuuren et al., 2011).

We use two scenarios, RCP 4.5 and RCP 8.5, which divide our simulations after 2005. RCP 4.5 is an mitigation scenario of anthropogenic emissions where radiative forcing reaches $4.5\ \mathrm{W\ m^{-2}}$ in 2100 (Thomson et al., 2011). In comparison, RCP 8.5 is a high emissions scenario of considerable increase of greenhouse gas emissions and concentrations, leading to a radiative
20 forcing of $8.5\ \mathrm{W\ m^{-2}}$ at the end of the 21st century (Riahi et al., 2011).
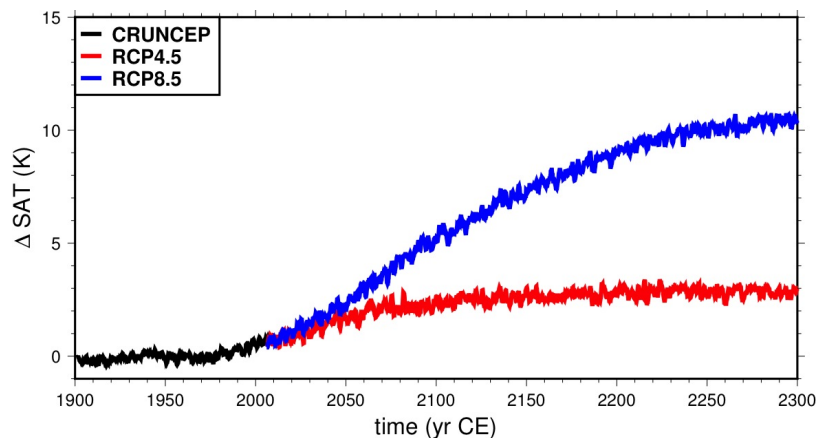

Figure 5. Mean SAT over land relative to the 20th century mean, from the CRUNCEP dataset (black) and the RCP 4.5 (red) and RCP 8.5 (blue) scenarios. Data taken from Viovy (2011); Thomson et al. (2011); Riahi et al. (2011).

Forcing datasets of monthly averages are provided by the Earth System Grid (NCAR, 2013) for both scenarios. To produce 6h-resolution datasets suitable for CLM4.5, we calculated the 6h-anomalies to monthly average for temperature and precipitation in the years 1996-2005 of the CRUNCEP dataset, and added this 10 yr series of anomalies to the monthly datasets cyclically, starting in 2006. The 6h-resolution datasets produced this way were then used to force the land system between

5   2006-2300 for the two scenarios. The mean SAT over the land area for the duration of our simulation time is shown in Fig. 5. The mean SAT at 2300 is ≈ 2 K higher than in 2005 for the RCP 4.5 scenario, while in the RCP 8.5 scenario temperature rises ≈ 9.5 K for the same period.

4   Results

4.1   Heat storage

10   #### 4.1.1   Effect of the depth of the bottom boundary

Given the continuous increase in mean SAT forcing seen in Fig. 5, we can expect the subsurface temperatures to behave as discussed in section 2. If the subsurface is shallow, the bottom boundary of the LSM reflects energy back to the surface instead of propagating it downwards. As explained in section 2, the total energy that is reflected back to the surface increases with time and decreases with the depth d of the bottom boundary. The obtained results are summarized in Table 1.

Table 1. Heat stored in the subsurface since 1901 CE at the years 2000, 2100, 2200 and 2300 CE for the RCP 4.5 and RCP 8.5 scenarios.

		RCP 4.5			RCP 8.5		
d (m)	ΔH 1901-2000 (ZJ)	ΔH 1901-2100 (ZJ)	ΔH 1901-2200 (ZJ)	ΔH 1901-2300 (ZJ)	ΔH 1901-2100 (ZJ)	ΔH 1901-2200 (ZJ)	ΔH 1901-2300 (ZJ)
42.1	6.03	24.14	26.91	27.74	44.41	78.13	92.64
92.1	7.31	41.12	53.91	57.84	69.90	148.01	191.37
142.1	7.63	45.96	69.59	81.52	75.65	178.98	255.66
192.1	7.66	46.81	75.02	93.67	76.59	187.63	282.66
242.1	7.66	46.94	76.35	98.15	76.73	189.52	291.36
292.1	7.66	46.95	76.67	99.60	76.74	189.89	293.77
342.1	7.66	46.96	76.75	100.00	76.72	189.92	294.31

15   Figure 6 shows how the heat absorbed by the subsurface varies with time between models of different subsurface thickness d. If the bottom boundary is too shallow, the thermal signal from the surface reaches the bottom boundary and further absorption of heat is hindered. For the original depth of the CLM4.5, $d = 42.1$ m, we see that after 100 yr its subsurface absorbs considerably less heat than for the deeper models. As we progressively increase the thickness of the subsurface, this effect is reduced and delayed. By the end of the simulation, the thickest model ($d = 342.1$ m) has absorbed 72 ZJ (72×10^{21} J) in the RCP 4.5

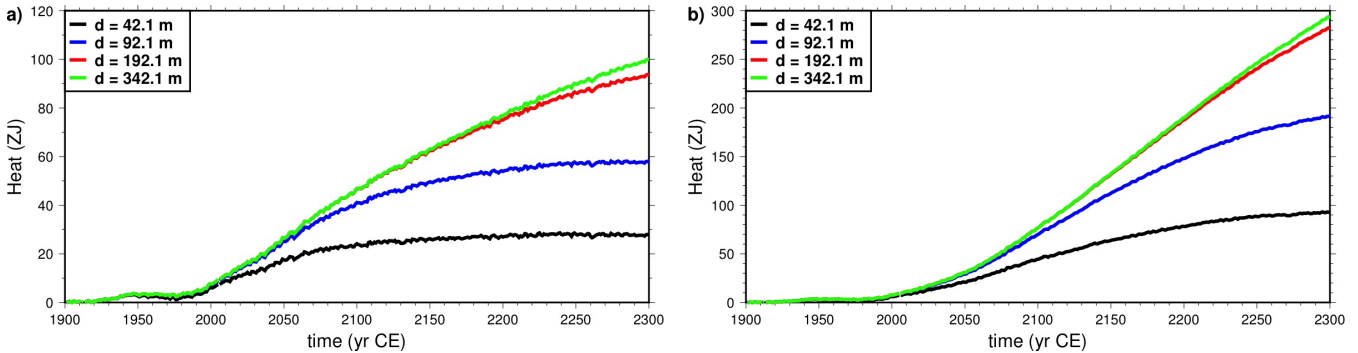Geoscientific
Model Development
Discussions

Figure 6. Heat stored in the subsurface as function of time, for models of subsurface thickness d of 42.1 m (black), 92.1 m (blue) 192.1 m (red) and 342.1 m (green). a) Simulations forced with CRUNCEP + RCP 4.5 data. b) Simulations forced with CRUNCEP + RCP 8.5 data. Note the scale difference between scenarios RCP 4.5 and RCP 8.5.

scenario and 201 ZJ in the RCP 8.5 scenario, which are respectively 260% and 217% of the heat stored by the thinnest model in these scenarios.
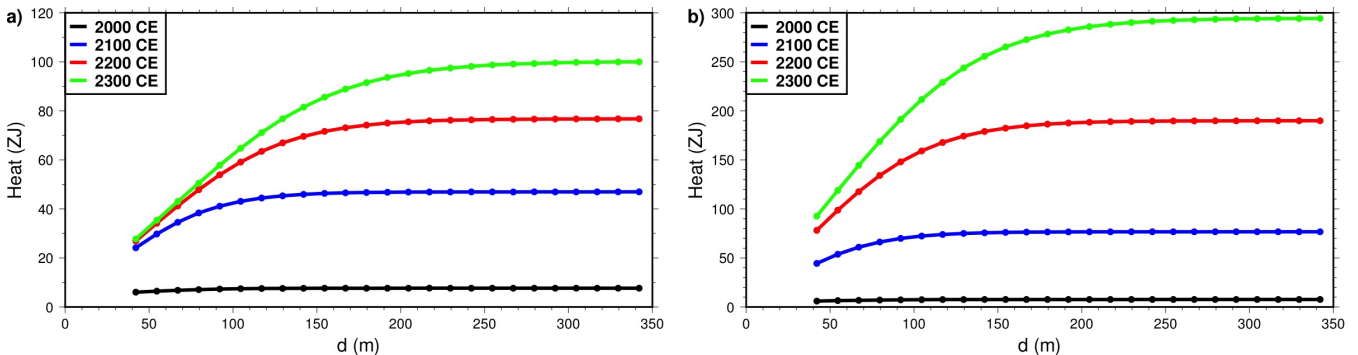
Figure 7. Heat stored in the subsurface as function of subsurface thickness, at the years 2000 (black), 2100 (blue), 2200 (red) and 2300 (green). a) Simulations forced with CRUNCEP + RCP 4.5 data. b) Simulations forced with CRUNCEP + RCP 8.5 data. Note the scale difference between scenarios RCP 4.5 and RCP 8.5.

The influence of d on the subsurface heat storage is clearly displayed in Fig. 7. At a given time, the heat absorbed by the subsurface increases with the depth of the bottom boundary d of the model. The amount of heat is not proportional to d and levels off when d increases past some value. This value is the thickness required by the model to keep the heat absorbed close to the maximum absorbed by the half space. If we define this threshold as 95%, this depth would be ≈ 90 m if the simulation runs for 100 yr (until 2000 CE). If we look at the heat absorbed after 400 yr, this threshold depth is ≈ 200 m in the RCP 4.5 scenario (Fig. 7a), and ≈ 180 m in the RCP 8.5 scenario (Fig. 7b). This difference shows that the SAT forcing, dependent on the scenario, has only a small influence on the threshold. It is mostly determined by the relationship $d \propto \sqrt{\kappa t}$ deduced from Eq. (5) for the perturbation to the thermal profile.
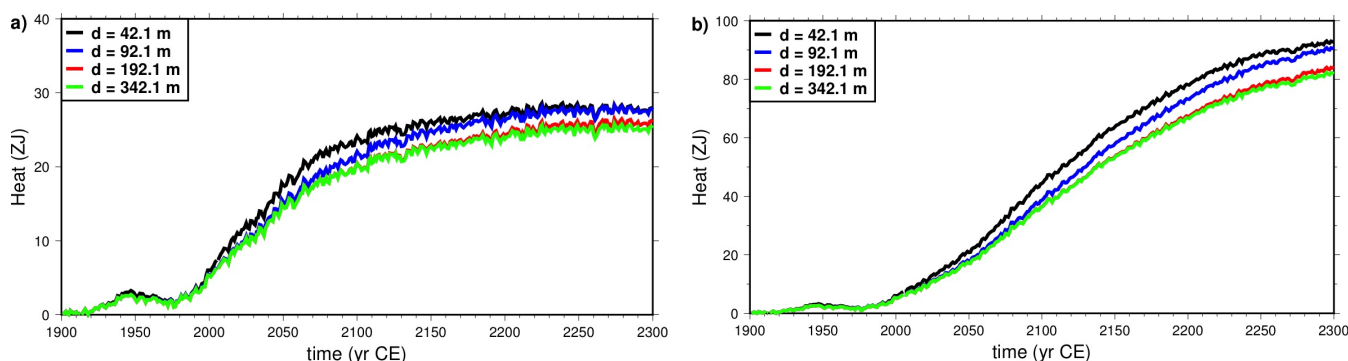
Figure 8. Heat stored in the upper 42.1 m as function of time, for models of subsurface thickness d of 42.1 m (black), 92.1 m (blue) 192.1 m (red) and 342.1 m (green). a) Simulations forced with CRUNCEP + RCP 4.5 data. b) Simulations forced with CRUNCEP + RCP 8.5 data. Note the scale difference between scenarios RCP 4.5 and RCP 8.5.

Deepening the bottom boundary below 42.1 m also affects the storage of heat within the layers above (Fig. 8). The thermal signal is reflected by the bottom boundary, further heating the region above, but as we increase d, this additional heat decreases. For the thickest model ($d = 342.1$ m), the upper 42.1 m of the subsurface gain 2.5 ZJ less than the thinnest model in the RCP4.5 scenario (Fig. 8a) and 10.7 ZJ in the RCP8.5 scenario (Fig. 8b), which correspond respectively to a decrease of 9% and of 11.6%.

Table 2. Heat stored in the soil (upper 3.8 m) since 1901 CE at the years 2000 and 2300 CE for the RCP 4.5 and RCP 8.5 scenarios.

			RCP 4.5		RCP 8.5	
d (m)	ΔH 1901-2000 (ZJ)	$\Delta H(d)/\Delta H(42.1)$ 1901-2000	ΔH 1901-2300 (ZJ)	$\Delta H(d)/\Delta H(42.1)$ 1901-2300	ΔH 1901-2300 (ZJ)	$\Delta H(d)/\Delta H(42.1)$ 1901-2300
42.1	1.831	1	4.473	1	10.532	1
92.1	1.816	0.9917	4.465	0.9984	10.471	0.9942
142.1	1.813	0.9904	4.441	0.9930	10.392	0.9867
192.1	1.817	0.9926	4.427	0.9898	10.348	0.9826
242.1	1.813	0.9904	4.419	0.9879	10.330	0.9809
292.1	1.810	0.9885	4.412	0.9864	10.332	0.9810
342.1	1.814	0.9908	4.411	0.9863	10.321	0.9800

Most of the subsurface is considered as bedrock, where the only heat transport process is thermal diffusion. The region of most interest is the soil, (upper 3.8m) where biogeochemical processes, sensitive to temperature, take place. The heat absorbed by the soil has been summarized in Table 2. Figure 9 shows that the heat absorbed by the soil is overestimated for the shallow bottom boundary variants of the model in the same manner as heat was for the upper 42.1 m, however this effect is much smaller.
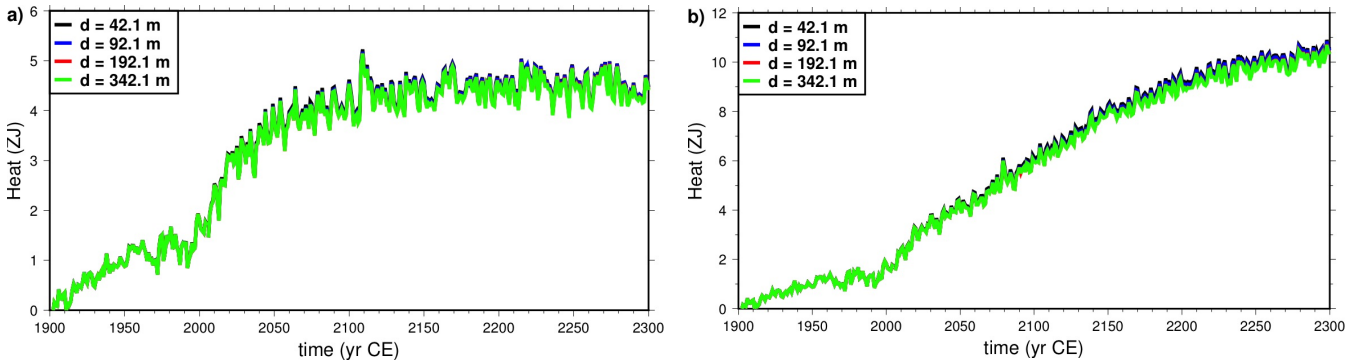
Geoscientific
Model Development
Discussions

Figure 9. Heat stored in the soil (upper 3.8 m), for models of subsurface thickness d of 42.1 m (black), 92.1 m (blue) 192.1 m (red) and 342.1 m (green). a) Simulations forced with CRUNCEP + RCP 4.5 data. b) Simulations forced with CRUNCEP + RCP 8.5 data. Note the scale difference between scenarios RCP 4.5 and RCP 8.5.
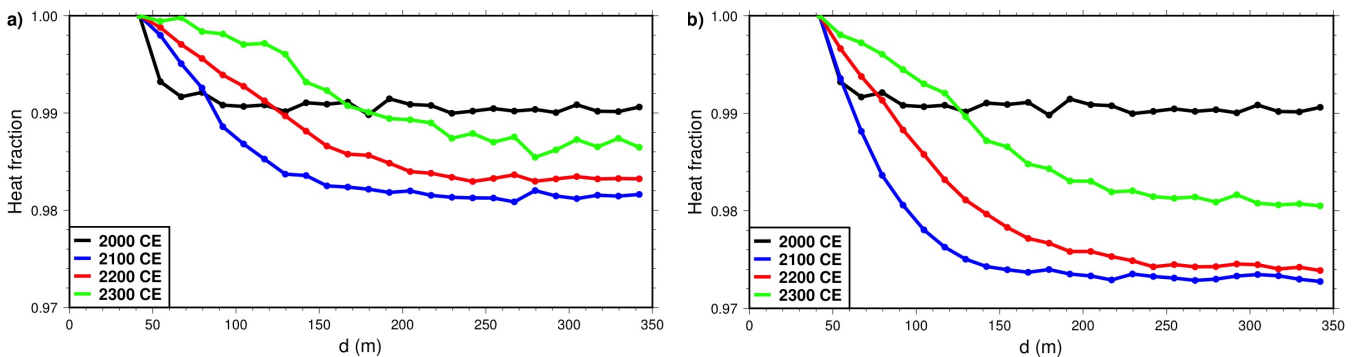

Figure 10. Heat stored in the soil as function of subsurface thickness, as fraction of that the thinnest model (d=42.1 m). Years 2000 (black), 2100 (blue), 2200 (red) and 2300 (green). a) Simulations forced with CRUNCEP + RCP 4.5 data. b) Simulations forced with CRUNCEP + RCP 8.5 data. Note the scale difference between scenarios RCP 4.5 and RCP 8.5.

The quantitative differences in Fig. 9 are small and better analyzed as the heat gained by the soil in each model as relative to the heat gained by the thinnest model (42.1 m thick) (Fig. 10). Compared to the thinnest model, the heat stored in the deepest models is $\approx 1\%$ less after 100 years of simulation, and $\approx 1.33\%$ at the end of the RCP 4.5 scenario (Fig. 10a) and $\approx 1.92\%$ at the end of the RCP 8.5 scenario (Fig. 10b). It can be noted that the relative decrease of heat gained by the soil in the deepest models is larger at 2100 CE than at either 2000 CE or 2300 CE. This, as well as for the differences between Figs. 10a and 10b, is caused by the yearly changes of SAT forcing (Fig. 5), which increases at the fastest rate during the 21st century in both RCP scenarios.

4.1.2 Effect of the bottom heat flux

In a purely conductive thermal regime of the subsurface, the magnitude of the heat flux used as bottom boundary condition does not affect heat diffusion. This is not the case for the soil, because the thermal properties of the soil depend on temperature

through the water/ice content. However, because of the shallowness of the soil, the geothermal gradient does not raise soil temperature sufficiently to affect heat propagation. Therefore, while the bottom heat flux increases the heat content of the subsurface, it should not affect its time evolution.
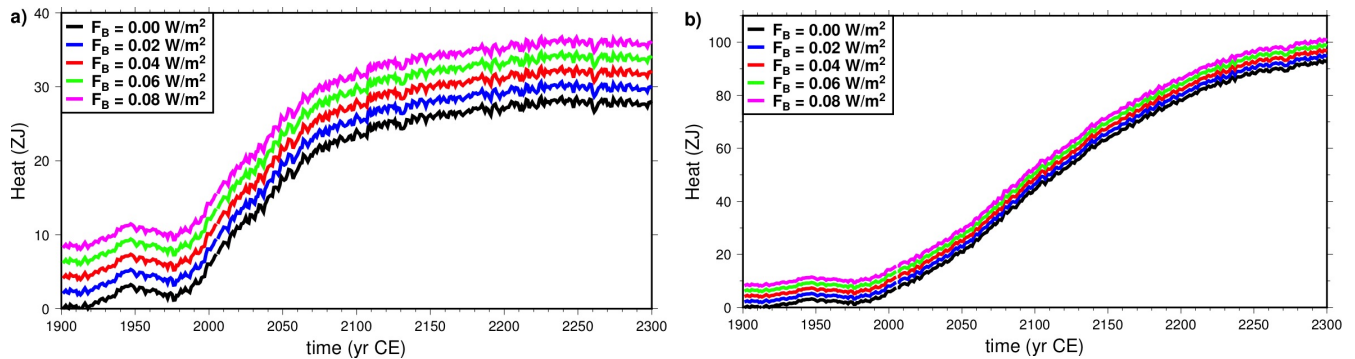

Figure 11. Heat stored in the upper 42.1 m (the thickness of all models is 42.1 m) as function of crustal heat flux, referenced to the initial heat content of the original model ($F_B = 0$ W m^{-2}). The heat content in each model is a static shift from that of the original model. a) Simulations forced with CRUNCEP + RCP 4.5 data. b) Simulations forced with CRUNCEP + RCP 8.5 data. Note the scale difference between scenarios RCP 4.5 and RCP 8.5.

The heat content within the subsurface as function of the bottom heat flux F_B is shown in Fig. 11. The bottom heat flux increases the heat content, adding 2.058 ± 0.006 ZJ for each 0.02 W m^{-2}. This offset is independent of the forcing scenario and constant in time.
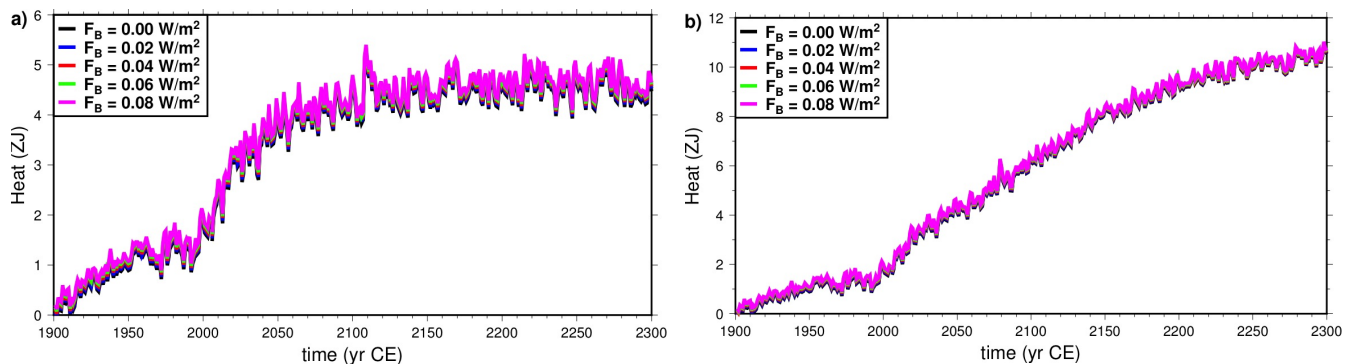

Figure 12. Heat stored in the soil (upper 3.8 m) as function of crustal heat flux, referenced to the initial heat content of the original model ($F_B = 0$ W m^{-2}). a) Simulations forced with CRUNCEP + RCP 4.5 data. b) Simulations forced with CRUNCEP + RCP 8.5 data. Note the scale difference between scenarios RCP 4.5 and RCP 8.5.

If we look at the heat content within soil (upper 3.8 m) we see the same behavior as for the upper 42.1 m but with smaller amplitude, as shown in Fig. 12. Heat content is offset by 0.043 ± 0.004 ZJ for every 0.02 W m^{-2} increase, regardless of the scenario.

Geoscientific
Model Development
Discussions

This increase of soil heat content due to the bottom heat flux does not translate into a uniform increase of soil temperature across individual cells, because soil composition and thermal properties vary. Each $0.02\ \mathrm{W\ m^{-2}}$ increase of bottom heat flux increases the temperature of the deepest soil layer (node at depth 2.86 m) by 0.04 ± 0.01 K. Using the mean continental heat flux $0.06\ \mathrm{W\ m^{-2}}$ as bottom boundary increases the temperature of the bottom soil layer by 0.12 ± 0.03 K and that of the bottom bedrock layer (node depth at 35.1 m) by 0.8 ± 0.04 K.

4.2 Permafrost

4.2.1 Intermediate-depth Permafrost
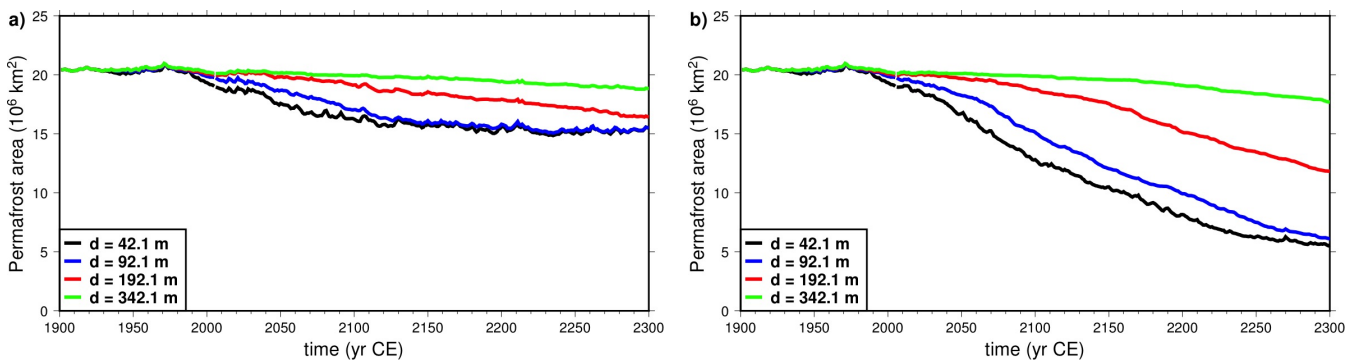
Figure 13. Northern Hemisphere intermediate-depth (0-42.1 m) permafrost area as function of time. Model versions with bottom boundary depth d at 42.1 m (black), 92.1 m (blue) 192.1 m (red) and 342.1 m (green). a) Simulations forced with CRUNCEP + RCP 4.5 data. b) Simulations forced with CRUNCEP + RCP 8.5 data.
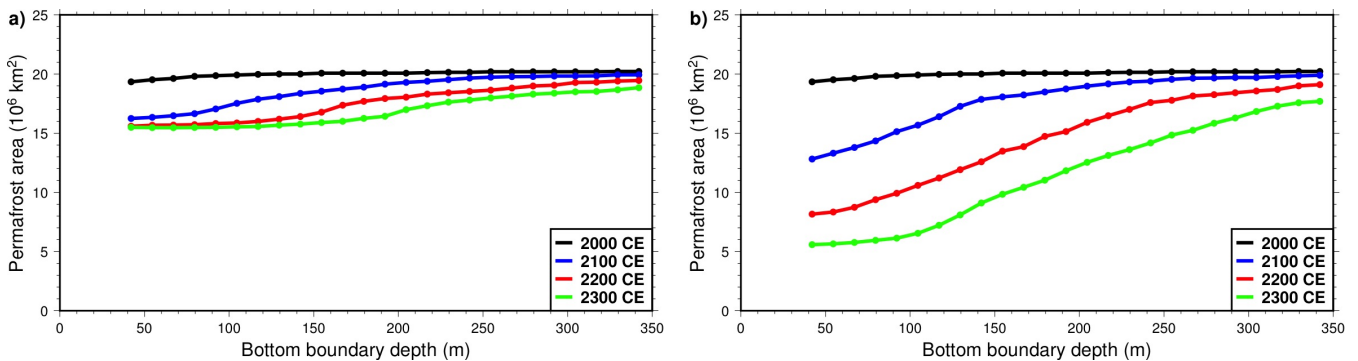

Figure 14. Northern Hemisphere intermediate-depth permafrost area as function of subsurface thickness d, at the years 2000 (black), 2100 (blue), 2200 (red) and 2300 (green). a) Simulations forced with CRUNCEP + RCP 4.5 data. b) Simulations forced with CRUNCEP + RCP 8.5 data.

17

Given the increasing SAT anomalies used to force the model (Fig. 5), we expect to observe a continuous decrease in the area extent of permafrost during the simulation period. The SAT warming signal is expected to propagate into the subsurface and, for an excessively shallow bottom boundary, be reflected back to the surface, thus overheating the subsurface. Increasing the depth of the bottom boundary attenuates this effect and therefore decreases the rate of permafrost thawing. Because a shallow

5   bottom boundary heats the subsurface from the bottom, this overheating is higher at the bottom of the subsurface, and the effect on the soil is less noticeable.

In our experiments, the area with intermediate-depth permafrost in the Northern Hemisphere (Fig. 13) has an initial extent of 20.4×10^6 km^2 in 1901. At the end of the RCP 4.5 scenario, this area has been reduced by 4.94×10^6 km^2 (24.1%) for the thinnest model and by 1.59×10^6 km^2 (7.8%) for the thickest model. For the RCP 8.5 scenario, the area losses of intermediate-

10 depth permafrost are 14.85×10^6 km^2 (72.7%) for the thinnest model and 2.74×10^6 km^2 (13.4%) for the thickest model.

For both scenarios, the decrease of intermediate-depth permafrost area becomes smaller as we increase the depth of the bottom boundary (Fig. 14). Each increase of the thickness of the subsurface produces diminishing returns, reaching a plateau where the permafrost area is not affected by a further increase of the bottom boundary depth. The depth at which this plateau is reached increases with the length of the simulation, and by the end of the simulations at 2300, it exceeds the largest bottom

15 boundary depth (342.1 m) used in our versions of the model.
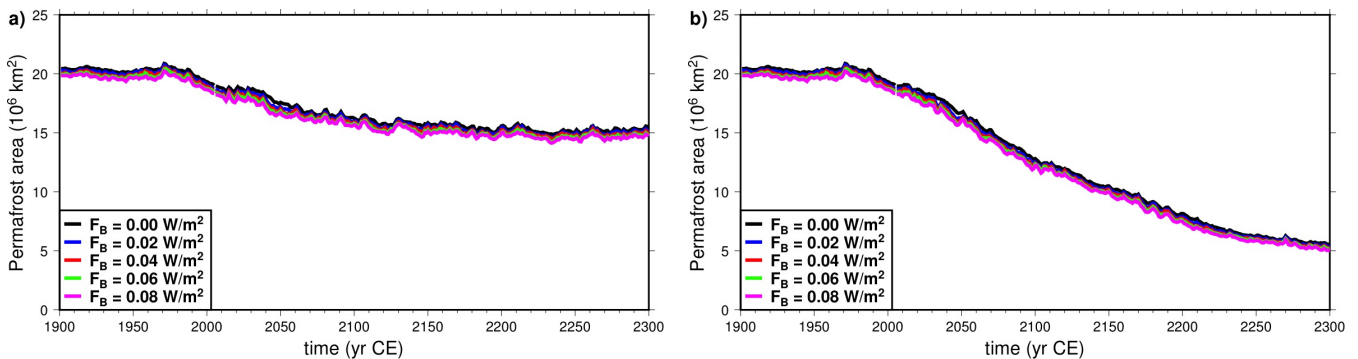

Figure 15. Northern Hemisphere intermediate-depth permafrost area as function of time. Model versions using different heat flux as bottom boundary. a) Simulations forced with CRUNCEP + RCP 4.5 data. b) Simulations forced with CRUNCEP + RCP 8.5 data.

The addition of a non-zero heat flux boundary condition at the LSM's bottom boundary has a small effect on intermediate-depth permafrost area (Fig. 15). The initial extent of intermediate-depth permafrost at 1901 appears reduced by $0.15 \pm 0.07 \times 10^6$ km^2 (0.7%) for every increase of 0.02 W m^{-2} in F_B. This difference does not remain constant during the simulation, each increase 0.02 W m^{-2} of F_B decreases the intermediate-depth permafrost area at the end of the simulation by $0.19 \pm 0.14 \times$

20 10^6 km^2 in the RCP 4.5 scenario (Fig. 15a) and by $0.12 \pm 0.05 \times 10^6$ km^2 in the RCP 8.5 scenario, a relative decrease of 1.2% and 2.1% respectively (Fig. 15b).

Geoscientific
Model Development
Discussions

Table 3. Areal extent of intermediate-depth permafrost at 1901 CE, 2000 CE and 2300 CE for the RCP 4.5 and RCP 8.5 scenarios.

Subsurface parameters		CRU-NCEP		RCP 4.5		RCP 8.5	
		PF area	PF area	PF area	Fraction	PF area	Fraction
		1901	2000	2300	PF lost	2300	PF lost
d (m)	F_B (W m^{-2})	($\times 10^6$ km^2)	($\times 10^6$ km^2)	($\times 10^6$ km^2)	1901-2300 (%)	($\times 10^6$ km^2)	1901-2300 (%)
42.1	0	20.43	19.33	15.49	24.18	5.58	72.68
42.1	0.08	19.85	18.65	14.72	25.84	5.11	74.25
342.1	0	20.43	20.21	18.84	7.78	17.69	13.41

4.2.2 Near-surface permafrost
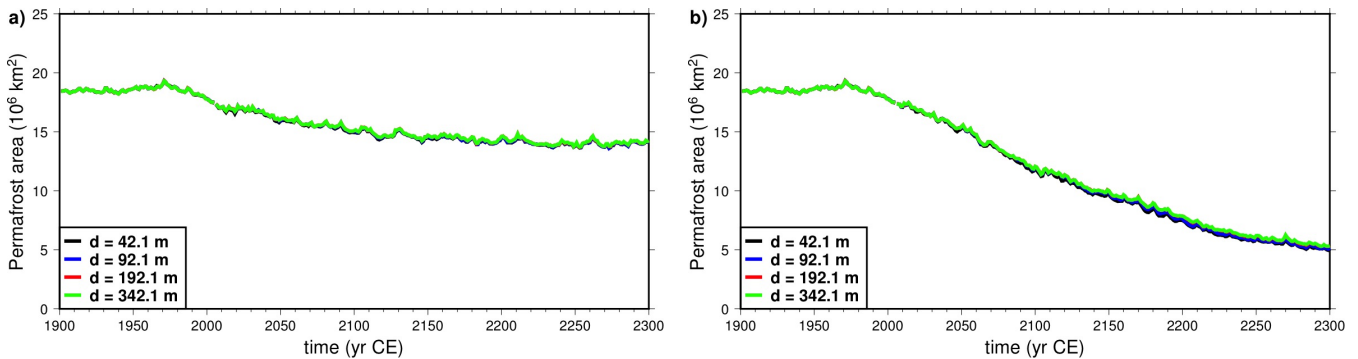
Figure 16. Northern Hemisphere near-surface permafrost area as function of time. Model versions with bottom boundary depth at 42.1 m (black), 92.1 m (blue) 192.1 m (red) and 342.1 m (green). a) Simulations forced with CRUNCEP + RCP 4.5 data. b) Simulations forced with CRUNCEP + RCP 8.5 data.

The near-surface permafrost (within the upper 3.8 m) area in the Northern Hemisphere is much less affected by the thickness of the model than the intermediate-depth permafrost (Fig. 16). The initial extent of near-surface permafrost is 18.45×10^6 km^2, and by 2300 under the RCP 4.5, this area has been reduced by 4.27×10^6 km^2 (23.1%) for the thinnest model and 4.20×10^6 km^2 (22.7%) for the thickest model, a relative difference of 1.6%. In the RCP 8.5 case, the permafrost area is reduced by 13.37×10^6 km^2 (72.5%) for the thinnest model and 13.11×10^6 km^2 (71.1%) for the thickest model, an area decrease 1.9% smaller.

The effect of the bottom heat flux F_B on near-surface permafrost area is similar to that on intermediate-depth permafrost, but quantitatively smaller (Fig. 17). Each 0.02 W m^{-2} increase reduces the initial near-surface permafrost extent by $0.05 \pm 0.04 \times 10^6$ km^2 (0.3%). At 2300, this difference is $0.09 \pm 0.8 \times 10^6$ km^2 (0.6%) for the RCP 4.5 scenario and $0.04 \pm 0.01 \times 10^6$ km^2 (0.8%) for the RCP 8.5 scenario (Fig. 17b).
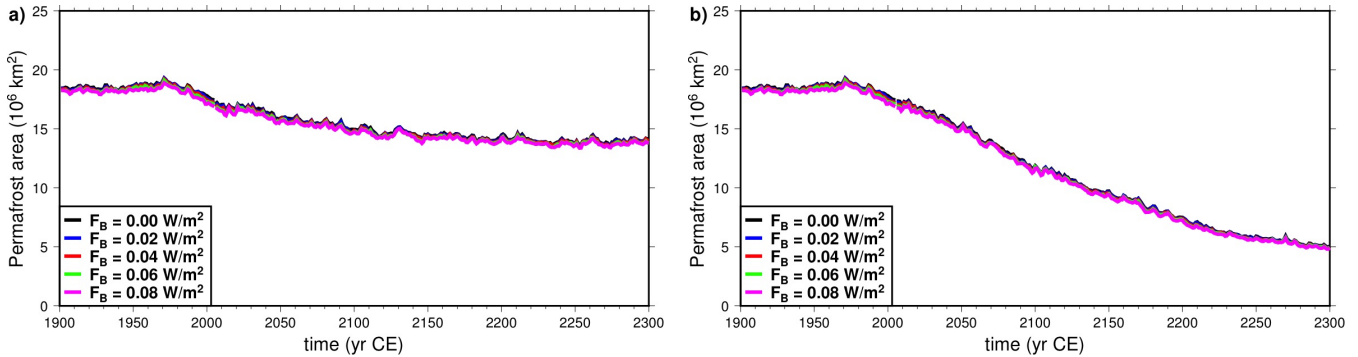
19

Figure 17. Northern Hemisphere near-surface permafrost area as function of time. Models using different heat flux as bottom boundary. a) Simulations forced with CRUNCEP + RCP 4.5 data. b) Simulations forced with CRUNCEP + RCP 8.5 data.
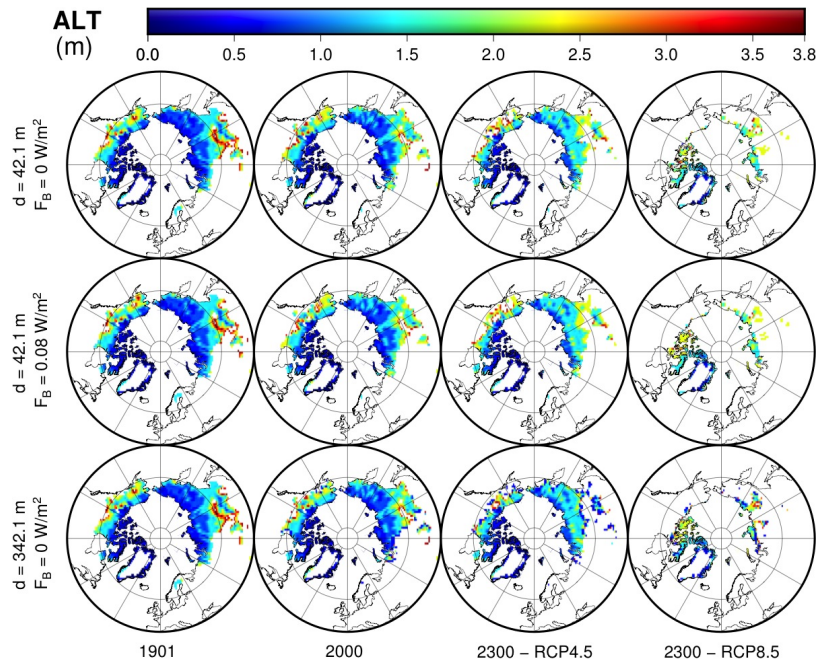

Figure 18. Active Layer Thickness for the unmodified model (top), the model with bottom heat flux 0.08 W m^{-2} (middle), and the model with bottom boundary depth $d = 342.1$ m (bottom). Time frames at 1901 CE, 2000 CE, and 2300 CE for the scenarios RCP 4.5 and RCP 8.5.

The initial state of the subsurface in 1901 is identical for model versions with different subsurface thickness. Differences in ALT between the thinnest and thickest models increase gradually over time, and in 2300 the ALT is visibly bigger for the thinnest model for both scenarios. The differences in ALT are bigger near the limits of the permafrost area, where the upper limit of permafrost is deeper (Fig. 18).

The bottom heat flux increases temperature proportional to the flux and the depth. Therefore, bottom heat flux does not alter ALT if permafrost is shallow. Where ALT is large, the increase in temperature due to the bottom heat flux is enough to induce thawing and lower the upper limit of permafrost (Fig. 18).

Table 4. Areal extent of near-surface permafrost at 1901 CE, 2000 CE and 2300 CE for the RCP 4.5 and RCP 8.5 scenarios.

Subsurface parameters		CRU-NCEP		RCP 4.5		RCP 8.5	
d (m)	F_B (W m^{-2})	PF area 1901 ($\times 10^6$ km^2)	PF area 2000 ($\times 10^6$ km^2)	PF area 2300 ($\times 10^6$ km^2)	Fraction PF lost 1901-2300 (%)	PF area 2300 ($\times 10^6$ km^2)	Fraction PF lost 1901-2300 (%)
42.1	0	18.45	17.8	14.17	23.17	5.07	72.49
42.1	0.08	18.25	17.09	13.80	24.40	4.90	73.15
342.1	0	18.45	17.5	14.25	22.75	5.34	71.07

4.3 Carbon
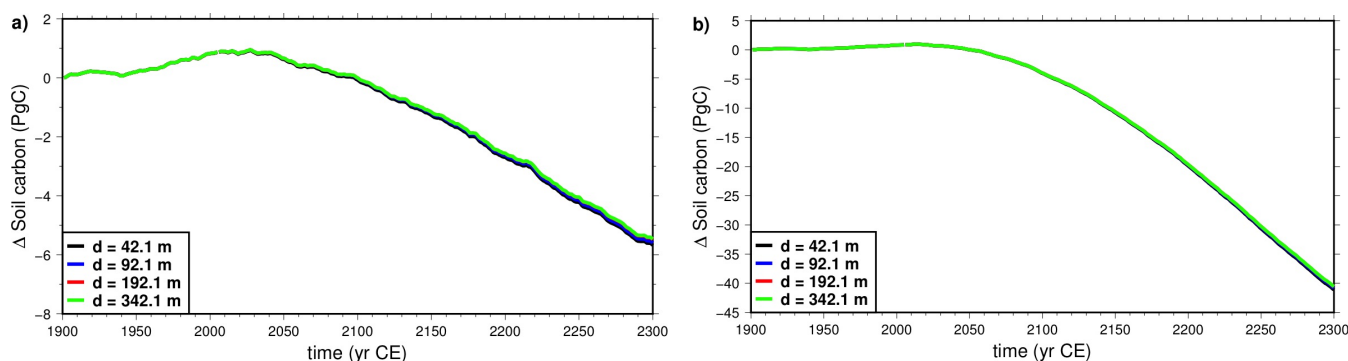
5 ### 4.3.1 Soil Carbon

Figure 19. Evolution of soil carbon pool in the Northern Hemisphere permafrost region, compared to the size for the original model at 1901 CE. Models with varying bottom boundary depth. a) Simulations forced with CRUNCEP + RCP 4.5 data. b) Simulations forced with CRUNCEP + RCP 8.5 data. Note different vertical scale in panel a and b.

The size of the soil carbon pool increases during the first ≈ 150 yr of simulation and thereafter begins decreasing. Increasing the depth of the bottom boundary reduces the loss of soil carbon, as expected because it slows the rate of permafrost thawing. The loss of soil carbon for the thickest subsurface (342.1 m) is 0.15 PgC (3.6%) less than for the thinnest subsurface model (42.1 m) in the RCP 4.5 scenario, and 0.56 PgC (1.3%) less in the RCP 8.5 scenario (Fig. 19).
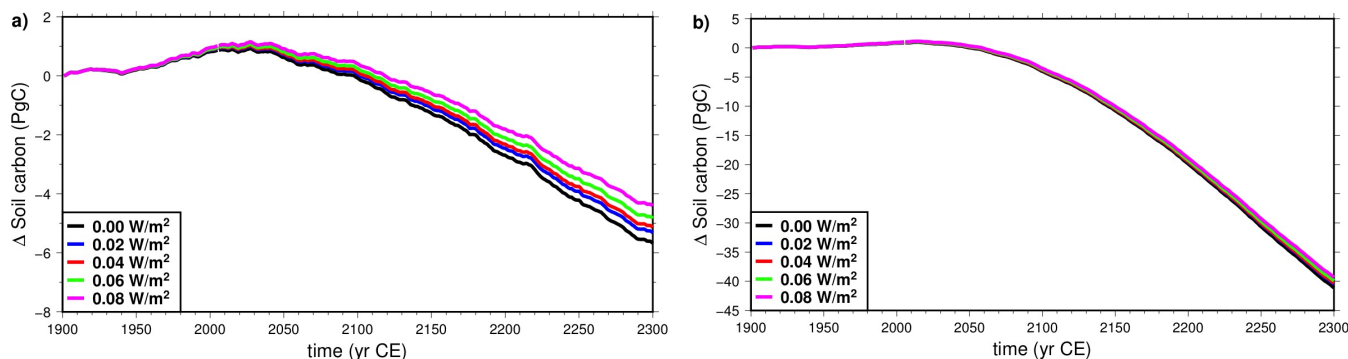
Geoscientific
Model Development
Discussions

Figure 20. Evolution of soil carbon pool in the Northern Hemisphere permafrost region, compared to the size for the original model at 1901 CE. Models with varying basal heat flux. a) Simulations forced with CRUNCEP + RCP 4.5 data. b) Simulations forced with CRUNCEP + RCP 8.5 data. Note different vertical scale in panel a and b.

Increasing the bottom heat flux F_B slows down the rate at which soil carbon in the permafrost region decreases during the simulation. An increase of 0.02 W m^{-2} decreases the loss of soil carbon between 1901 and 2300 and by 0.3 ± 0.1 PgC (5.6%) in the RCP 4.5 scenario and 0.45 ± 0.2 PgC (1.1%) in the RCP 8.5 scenario (Fig. 20).

The regional distribution of soil carbon can be found in Fig. 21. For the original model, the biggest concentrations of soil carbon are located in the permafrost regions of the northern hemisphere, mainly in Alaska and Eastern Siberia. Because the changes in soil carbon due to the modification of model thickness of bottom heat flux are very small relative to the size of the pool, we have represented the difference in soil carbon to the original model for the modified models of increased thickness $d = 342.1$ m and bottom heat flux $F_B = 0.08$ W m^{-2}. While model versions of different thickness share a common initial state, over time increasing the thickness of the model has the effect of increasing soil carbon concentration across the region.

Models with different bottom heat flux F_B depart from different initial conditions (since the bottom heat flux determines the thermal steady state of the subsurface). We can see that increasing F_B decreases the initial concentration of soil carbon in some areas while increasing it in others. These differences can be of the same order of magnitude as the carbon concentration in the original model in token gridcells. Some cells have quantities of soil carbon in the $F_B = 0.08$ W m^{-2} model half of that of the original model, while other have 10 times as much. As these differences have different sign, the effect on the whole region is proportionally much smaller (Fig. 21).

Figure 22 shows the initial size of the soil carbon pool in the Northern Hemisphere permafrost region for models with different bottom heat flux. The absence of a consistent trend in the size of the soil carbon pool as we increase the bottom heat flux is due to the regional variability seen in Fig. 21, since the soil carbon in each gridcell can either increase or decrease due to the basal heat flux.
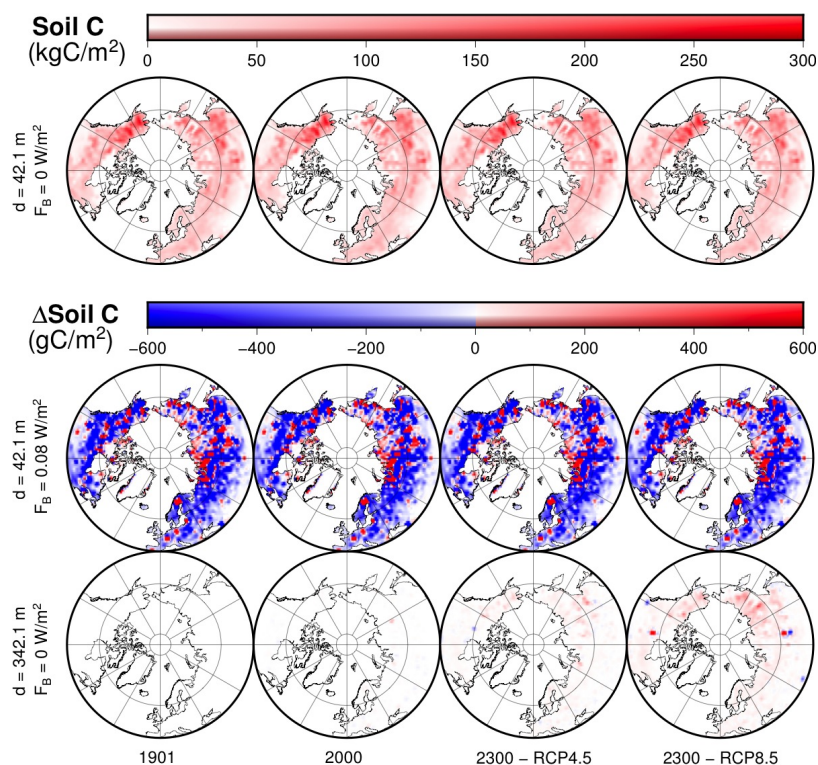
Geoscientific
Model Development
Discussions

Figure 21. Distribution of soil carbon for the original model (top), and differences to the original model at each time frame for the modified model with $F_B = 0.08$ W m^{-2} (middle) and the modified model with $d = 342.1$ m (bottom). Time frames at 1901 CE, 2000 CE, and 2300 CE for the scenarios RCP 4.5 and RCP 8.5.

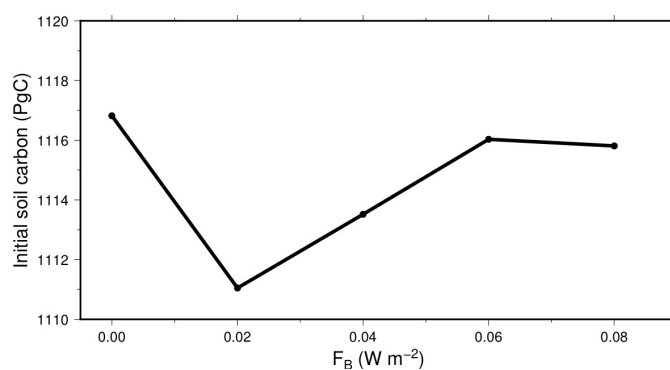**Figure 22.** Mean size of the soil carbon pool in the Northern Hemisphere permafrost region between 1901-1910, as function of basal heat flux.

Geoscientific
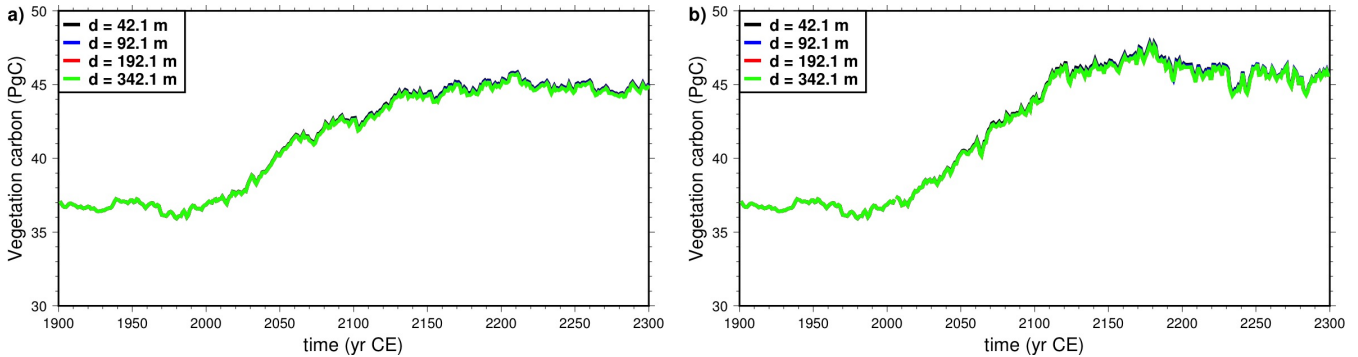Model Development
Discussions

Figure 23. Vegetation carbon pool in the Northern Hemisphere permafrost region. Models with varying bottom boundary depth. b) Simulations forced with CRUNCEP + RCP 8.5 data.

4.3.2 Vegetation Carbon

The vegetation carbon in the Northern hemisphere is also affected by the depth of the bottom boundary. Because rising temperatures allow plants to colonize higher latitudes, the vegetation increases for both RCP scenarios, reaching a stable level during the last two centuries (Fig. 23). While the models with different depth of the bottom boundary d depart from the same initial state at 1901, increasing the thickness of the model leads to slightly smaller masses of vegetation carbon. For the thickest model (342.1 m), the pool of vegetation carbon is 0.17 ± 0.01 PgC smaller during the last two centuries of simulation than it is for the thinnest model (42.1 m) for the RCP 4.5 scenario, and 0.11 ± 0.08 PgC smaller for the RCP 8.5 scenario.
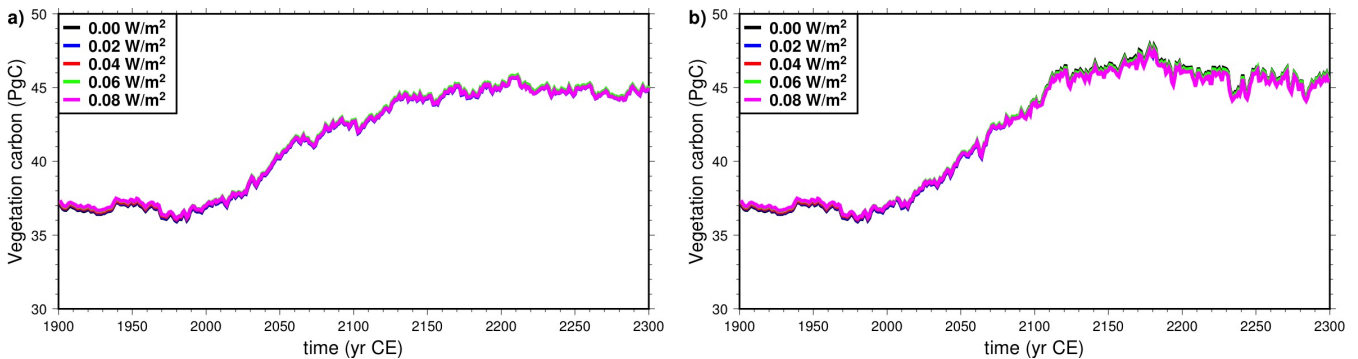

Figure 24. Vegetation carbon pool in the Northern Hemisphere permafrost region. Models with varying basal heat flux. a) Simulations forced with CRUNCEP + RCP 4.5 data. b) Simulations forced with CRUNCEP + RCP 8.5 data.

The bottom heat flux also has a small effect in the evolution of vegetation carbon in the Northern Hemisphere (Fig. 24) for both RCP scenarios. The average vegetation carbon between 2100-2300 for the model with $F_B = 0.08$ W m^{-2} is 0.35 ± 0.03

PgC less for the RCP 4.5 scenario and 0.54 ± 0.05 PgC less for the RCP 8.5 scenario than for the model with zero basal heat flux, a relative decrease of $0.8 \pm 0.08\%$ and $1.2 \pm 1\%$ respectively.
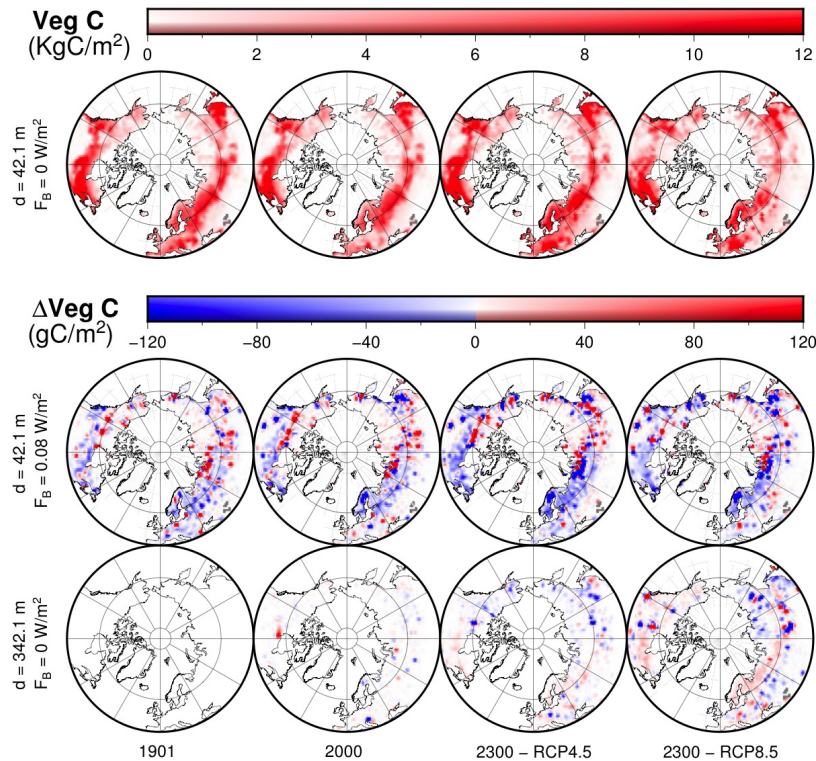

Figure 25. Distribution of vegetation carbon for the original model (top), and differences to the original model at each time frame for the modified model with $F_B = 0.08 \ \mathrm{W \ m^{-2}}$ (middle) and the modified model with $d = 342.1$ m (bottom). Time frames at 1901 CE, 2000 CE, and 2300 CE for the scenarios RCP 4.5 and RCP 8.5.

Figure 25 shows the regional distribution of vegetation carbon for the original model, and the difference between the original model and the modified versions of increased thickness $d = 342.1$ m and bottom heat flux $F_B = 0.08 \ \mathrm{W \ m^{-2}}$. Increasing d

5 and F_B results in a larger amount of vegetation carbon in some areas and a smaller quantity in others. At the end of the simulation, the effect is a net decrease of vegetation in the Northern Hemisphere for both RCP scenarios. There are differences in vegetation carbon at the start of the simulation in 1901 CE, where the increase in vegetation carbon with F_B is dominant.

The initial size of the vegetation carbon pool depends on the bottom heat flux. Fig. 26 shows how the bottom heat flux affects the mean of the vegetation carbon in the Northern Hemisphere permafrost region during the years 1901-1910 (used for

10 the spinup period). There is a consistent linear increase of 0.066 ± 0.02 PgC of the initial vegetation for each $0.02 \ \mathrm{W \ m^{-2}}$ increase of the bottom heat flux.
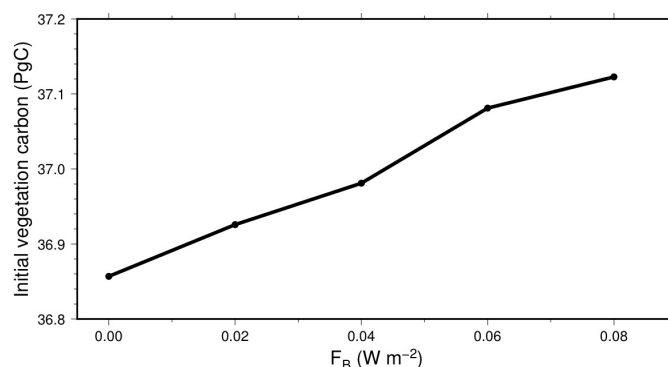
Figure 26. Mean size between 1901-1910 of the vegetation carbon pool in the Northern Hemisphere permafrost region, for models of different bottom heat flux.

4.3.3 Methane

Methane is produced by methanogenic microbes in the anaerobic fraction of soil. Therefore, it concentrates in areas where the water table rises high enough to reach the carbon-rich soil near the surface, or in inundated areas. The production of methane in natural wetlands is mainly located in the tropical areas, responsible for 64%-88% of the global wetland production (O'Connor et al., 2010).

In our CLM4.5-BGC simulations, most of the methane production is concentrated in the high-latitude wetlands (Fig. 27). In contrast, the tropical wetlands produce almost no methane. The reason is that the tropical areas do not get inundated and the water table remains low, never reaching the higher soil layers where most soil carbon is concentrated, even during the monsoon season. The water table remains low due to flaws in the hydrology model of CLM4.5, which we discuss later. High-latitude areas have low water tables as well, but get partially inundated during the year because the soil is frozen (impeding the filtration of water), and can produce methane.

In the Northern Hemisphere there are significant differences in the production of methane due to the bottom heat flux and the depth of the bottom boundary. These differences occur in a few areas where the difference in methane production can be within 50-80% of that of the original model. However, as the sign of these differences can be either positive or negative, the net effect over methane production is less pronounced.

As shown in Figs. 28 and 29, the net effect of the subsurface thickness and the bottom heat flux on the global methane production is much smaller than for the localized areas displayed in Fig. 27. Increasing the thickness of the model from 42.1 m to 342.1 m can result in increases and decreases of global methane production during the simulation between 0.1 to $0.2 \, \mathrm{TgC \, yr^{-1}}$ ($1 \, \mathrm{TgC} = 10^{12}$ g of C), only 0.3-0.5%. The bottom heat flux has a slightly larger effect, as a bottom heat flux of $F_B = 0.08 \, \mathrm{W \, m^{-2}}$ decreases methane production by 0.6 to $1.0 \, \mathrm{TgC \, yr^{-1}}$, a relative decrease of 1-1.6%.

Geoscientific
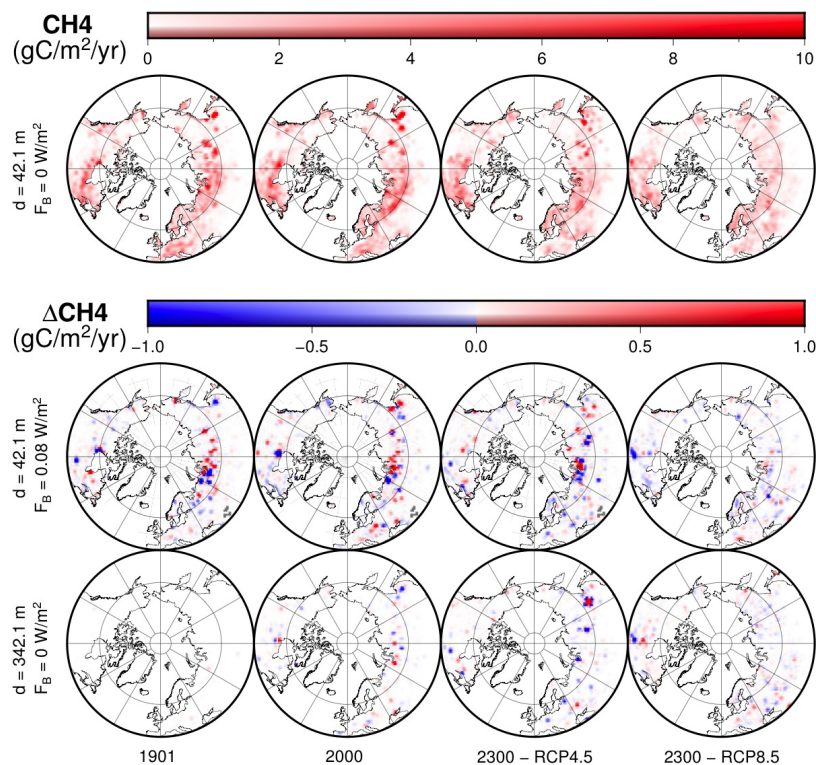Model Development
Discussions
Open Access

Figure 27. Distribution of methane yearly production for the original model (top), and differences to the original model at each time frame for the modified model with $F_B = 0.08$ W m^{-2} (middle) and the modified model with $d = 342.1$ m (bottom). Time frames at 1901 CE, 2000 CE, and 2300 CE for the scenarios RCP 4.5 and RCP 8.5.
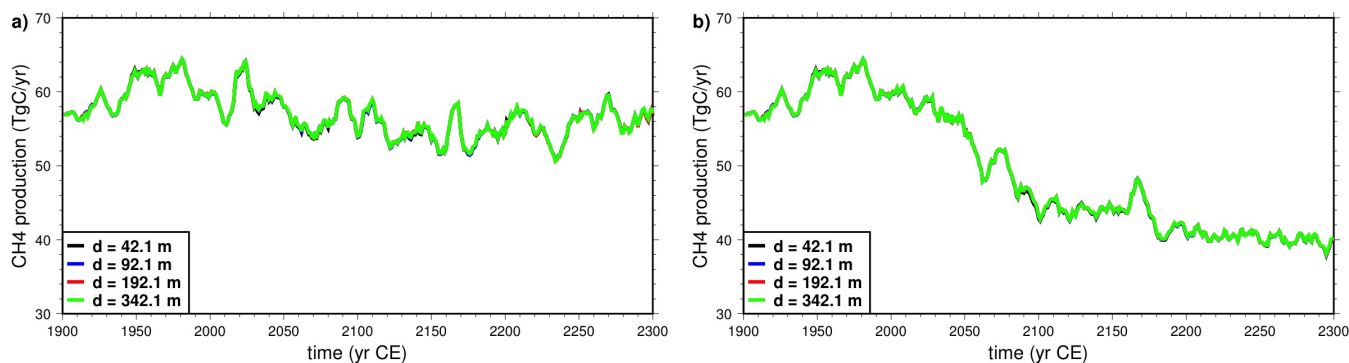

Figure 28. Global yearly methane production as function of time, moving average of 10 years. Models with varying bottom boundary depth. a) Simulations forced with CRUNCEP + RCP 4.5 data. b) Simulations forced with CRUNCEP + RCP 8.5 data.
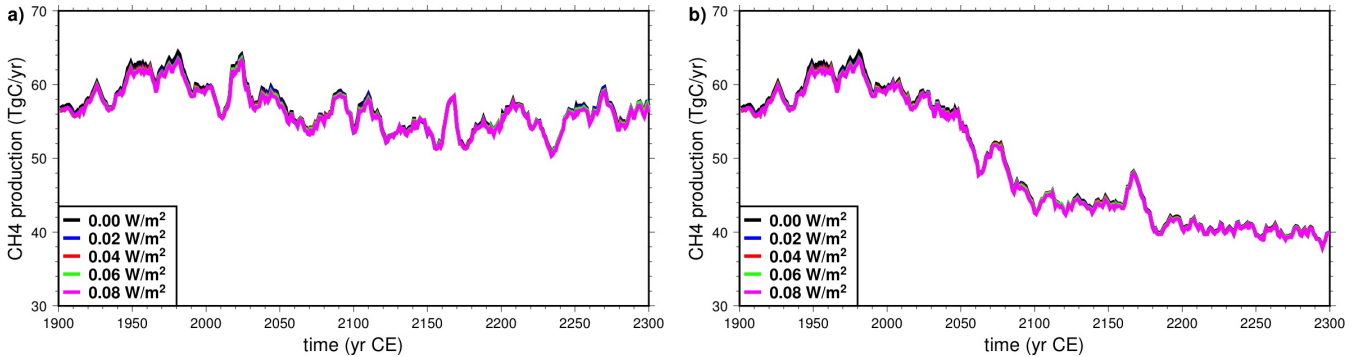
Figure 29. Global yearly methane production as function of time, moving average of 10 years. Models with varying basal heat flux. a) Simulations forced with CRUNCEP + RCP 4.5 data. b) Simulations forced with CRUNCEP + RCP 8.5 data.

5   Discussion and conclusions

Our results show that deepening the bottom boundary by 300 m increases the heat stored in the subsurface by 72 ZJ and 201 ZJ at the end of the simulations at 2300 CE for the two scenarios, which correspond respectively to 260% and 217% of the heat stored by the original shallow model. Heat absorption within the soil (upper 3.8 m) is reduced by 1-3% depending on the scenario and the length of the simulation. Increasing the bottom heat flux by 0.02 W m^{-2} raises the temperature at the bottom of the soil (3.8 m deep) by 0.04 ± 0.01 K, with some differences between cells due to the variable thermal properties of soil. Using the mean continental heat flux 0.06 W m^{-2} (Jaupart and Mareschal, 2010) increases the bottom soil temperature by 0.12 ± 0.03 K, and the temperature at the base of the model (42.1 m deep) by 0.8 ± 0.04.

Permafrost is affected by the depth of the bottom boundary, in a degree that depends on the depth to which we consider permafrost, in the same manner as the heat absorption by the subsurface. Permafrost near the surface is only slightly affected, but as we increase the depth to which we consider permafrost, the differences made by the thickness of the model became more and more significant. As Fig. 13 shows, the area loss of intermediate-depth permafrost is reduced by a factor of 3 in the RCP 4.5 scenario and by a factor of 5.5 in the RCP 8.5 scenario. The effect of the crustal heat flux in permafrost grows linearly with the magnitude of the heat flux and the depth of the permafrost, but even a bottom heat flux of $F_B = 0.08$ W m^{-2} only reduces intermediate-depth permafrost extent by 1-2%.

Increasing the depth of the bottom boundary leads to less vegetation and more soil carbon in the Northern Hemisphere permafrost region at the end of the simulations. This is to be expected, as the increasing the depth of the subsurface leads to reduced permafrost loss, which opens less area to vegetation and exposes less soil carbon to microbial activity. These effects are small, as the stable vegetation level reached between 2100-2300 in the thickest model is only reduced by 0.8-1.2% compared to the thinnest model, while soil carbon is reduced by 1.3-3.6%.

A higher basal heat flux has a regionally variable effect across the Northern Hemisphere, increasing soil carbon and vegetation where near-surface permafrost is present, but decreasing both outside of the permafrost region. The loss of soil carbon

in the permafrost region is 4-22% smaller with $F_B = 0.08$ W m^{-2} than with zero basal heat flux, while the initial quantities of carbon can range from half to 10 times as much in individual gridcells. This heat flux also reduces by 0.8-1.2% the stable vegetation level in this region during the last two centuries of the simulation. On the other hand, the bottom heat flux reduces methane production within areas where permafrost is present but increases it where soil only freezes seasonally.

5   In CLM4.5 subsurface biogeochemistry only takes place within the soil, the upper 3.8 m. For this reason, the small effect of the bottom boundary depth on near-surface permafrost translates into a small effect on the soil carbon and vegetation pools and the methane production. While the same could be expected from the basal heat flux, it has a varied effect across the Northern Hemisphere, specially in the areas where seasonal freezing of the soil occurs, but no soil permafrost is present.

While CLM4.5 uses as uniform soil thickness value of 3.8 m, natural soil thickness varies significantly, with an estimated
10   global mean of ≈ 13 m and reaching depths of several hundred meters in some areas (Shangguan et al., 2017). Soil affected by permafrost is therefore much deeper than in CLM4.5, and future models should use realistic maps of soil thickness, which makes the results obtained for intermediate-depth permafrost relevant. The uniform soil thickness also affects the hydrology model in CLM4.5, which in addition to the use of a virtual aquifer of 5 m, makes the hydrology model unrealistic. The new version 5.0 of CLM includes a spatially variable soil thickness within a range of 0.4 m to 8.5 m and eliminates the virtual
15   aquifer, which address the issues of the hydrology model in CLM4.5 (Lawrence et al., 2018).

The increased depth of soil in some areas imply that the effect of the basal heat flux and the bottom boundary depth would be bigger than our estimations, made for a soil depth of 3.8 m. While soil carbon pools in the permafrost region concentrate within the upper 3 m, additional reserves exist below 3 m which contain $\sim 60\%$ as much carbon as the upper 3 m (Hugelius et al., 2014). If considered in the model, these reserves would be more severely affected by the depth of the bottom boundary
20   and the bottom heat flux than the shallow carbon deposits are.

The methane production in CLM4.5-BGC is dependent on the hydrology model used in CLM4.5, which keeps the water table too low in the tropical regions of the Earth where most (64%-88%) wetland methane is produced (O'Connor et al., 2010). The consequence is that no methane is produced in these regions, and all methane is produced in the Northern Hemisphere where frozen soil can be inundated. Compared to the original model, a bottom heat flux of $F_B = 0.08$ W m^{-2} produces a
25   reduction of 1-1.6% across the whole permafrost region, while deepening the bottom boundary to 342.1 m only produces variations smaller than 0.5%. However, there can be differences as high as 50-80% respect to the original model, located in individual cells near the permafrost frontier. The lack of methane production in tropical regions associated to the hydrology should not be expected to occur in CLM5.0, which addresses the lack of realism of the hydrology model in CLM4.5.

The depth of the bottom boundary has a considerable effect on the heat absorbed by the subsurface. We have shown that, in
30   a simulation spanning 400 years, the LSM requires a thickness of at least 200 m to correctly estimate the temperature profile. The thickness d needed increases with the length t of the simulation, but this is not prohibitive for simulations running on much longer timescales, because the depth of the bottom boundary follows a square-root relation $d \propto \sqrt{\kappa t}$. Longer simulations such as the 1000 yr long simulations of the last millennium ensemble (Stocker et al., 2013), require subsurface thicknesses of $\sim 300 - 350$ m. The computational costs associated to each additional layer are almost negligible when compared to the whole
35   LSM, because the only process taking place in bedrock is thermal diffusion. We also used a fixed thickness for the additional

layers, but if we keep the original scheme where layer thickness increase exponentially, it is possible to increase the thickness of the model to hundreds of meters by adding only a few layers.

Any LSM, before a simulation starts, must be initialized with appropriate initial conditions, i.e. an initial state of the model that resembles the reality at the time. An appropriate initial condition for the temperature of the subsurface is the steady

5   state determined by the surface temperatures at the start of the simulation. This state can be reached during the length of the spinup from arbitrary initial temperatures, if the depth of the bottom boundary is much shallower than the depth determined by the relation $d \propto \sqrt{\kappa t}$, being t the length of the spinup. However, if we increase d enough to prevent the bottom boundary from affecting the thermal diffusion during the length of the simulation, we may also prevent those arbitrary initial temperatures reaching a steady state during the length of the spinup. This problem can be avoided if the spinup does not depart from arbitrary

10 initial subsurface temperatures, but instead from a temperature profile as close as possible to the steady state. As the steady state is determined by Eq. (6), it is possible to obtain an appropriate initial temperature profile by ignoring the time-varying perturbation T_t in this equation.

The thermal anomalies associated with insufficient depth of the bottom boundary and lack of basal heat flux are considerable throughout the subsurface. However, this effect is of little importance within the global heat budget model, as the heat

15 absorbed by the continents is less than even the uncertainty of heat absorption by the oceans (Rhein et al., 2013). The most important consequences are those on the carbon pools and fluxes in the North Hemisphere. These effects are not distributed homogeneously across the region, but located in small areas across the region. These areas are those where permafrost is the most affected by the bottom boundary depth and the basal heat flux, or that are located just outside the limit of the region where soil permafrost exists, which suggests that seasonal soil freezing also affects the carbon pools significantly. Methane

20 production can variate within one order of magnitude due to the changes to model thickness and basal heat flux.

Code availability

The modified CLM4.5 software, as well as the instructions for its use in a functional CLM4.5 installation, are available in the Zenodo repository (Hermoso de Mendoza, 2018).

Data availability

25 The dataset used to produce the initial conditions used in the simulations can be found in the Zenodo repository (Hermoso de Mendoza, 2018). Implementation of these initial conditions requires modifications to the software, which can be found in the same package.

Three datasets are used as boundary conditions for the simulations (i.e. the atmospheric datasets used to force the land model). The CRUNCEP dataset used to force the model between 1901-2005 is available in the NCAR-UCAR Research Data

30 Archive (Viovy, 2018). The two datasets used to force the model between 2006-2300, RCP 4.5 and RCP 8.5, are available in the Earth System Grid repository (NCAR, 2013).

Geoscientific
Model Development
Discussions

Acknowledgements

Acronyms

10 **ALT** Active Layer Thickness. 9, 20, 21

BGC BioGeoChemistry. 6–9, 26, 29

CESM1.2 Community Earth System Model version 1.2. 6, 9

CLM4 Community Land Model version 4. 7

CLM4.5 Community Land Model version 4.5. 3–10, 12, 26, 29

15 **CMIP5** fifth phase of the Climate Model Intercomparison Project. 2, 3

CN Carbon-Nitrogen. 7

CRU-TS Climate Research Unit Time-Series. 11

ESM Earth System Model. 1, 2, 6

LSM Land Surface Model. 2, 6, 8, 9, 11, 12, 18, 29, 30

20 **NCEP** National Centers for Environmental Prediction. 11

RCP Representative Concentration Pathway. 11–16, 18, 19, 21, 22, 24, 25, 28

SAT Surface Air Temperature. 6, 11–13, 15, 18

Geoscientific
Model Development
Discussions

References

Avis, C. A., Weaver, A. J., and Meissner, K. J.: Reduction in areal extent of high-latitude wetlands in response to permafrost thaw, Nature Geoscience, 4, 444, doi:10.1038/NGEO1160, 2011.

Beltrami, H., Smerdon, J., Pollack, H. N., and Huang, S.: Continental heat gain in the global climate system, Geophysical Research Letters, 2002.

B.Kirtman, Power, S., Adedoyin, J., Boer, G., Bojariu, R., Camilloni, I., Doblas-Reyes, F., Fiore, A., Kimoto, M., Meehl, G., Prather, M., Sarr, A., Schär, C., Sutton, R., van Oldenborgh, G., Vecchi, G., and Wang, H.: Near-term Climate Change: Projections and Predictability, chap. 11, Cambridge University Press, 2013.

Bonan, G.: Forests and climate change: forcings, feedbacks, and the climate benefits of forests, Science, 2008.

Bonan, G., Drewniak, B., Huang, M., et al.: Technical Description of Version 4.5 of the Community Land Model (CLM), Tech. rep., NCAR Technical Note NCAR/TN-503+ STR, Boulder, Colorado, 2013.

Carmichael, V. R. G.: Global and regional climate changes due to black carbon, Natural Geoscience, 2008.

Carslaw, H. S. and Jaeger, J. C.: Conduction of heat in solids, Oxford: Clarendon Press, 1959, 2nd ed., 1959.

Clauser, C. and Huenges, E.: Thermal conductivity of rocks and minerals, Rock physics & phase relations: a handbook of physical constants, pp. 105–126, 1995.

Cubasch, U., Wuebbles, D., Chen, D., Facchini, M., Frame, D., Mahowald, N., and Winther, J.-G.: Introduction, chap. 1, Cambridge University Press, 2013.

Cuesta-Valero, F. J., García-García, A., Beltrami, H., and Smerdon, J. E.: First assessment of continental energy storage in CMIP5 simulations, Geophysical Research Letters, 43, 5326–5335, doi:10.1002/2016GL068496, 2016.

Hansen, J. and Nazarenko, L.: Soot climate forcing via snow and ice albedos, Proceedings of the National Academy of Sciences of the United States of America, 2004.

Harris, I., Jones, P., Osborn, T., and Lister, D.: Updated high-resolution grids of monthly climatic observations–the CRU TS3. 10 Dataset, International Journal of Climatology, 34, 623–642, doi:10.1002/joc.3711, 2014.

Hermoso de Mendoza, I.: Lower boundary conditions improvement in CLM4.5, doi:10.5281/zenodo.1420497, https://zenodo.org/record/1420497, 2018.

Hugelius, G., Strauss, J., Zubrzycki, S., Harden, J. W., Schuur, E., Ping, C.-L., Schirrmeister, L., Grosse, G., Michaelson, G. J., Koven, C. D., et al.: Estimated stocks of circumpolar permafrost carbon with quantified uncertainty ranges and identified data gaps, Biogeosciences, 11, 6573–6593, doi:10.5194/bg-11-6573-2014, 2014.

Jaupart, C. and Mareschal, J.-C.: Heat generation and transport in the Earth, Cambridge university press, 2010.

Kalnay, E., Kanamitsu, M., Kistler, R., Collins, W., Deaven, D., Gandin, L., Iredell, M., Saha, S., White, G., Woollen, J., et al.: The NCEP/NCAR 40-year reanalysis project, Bulletin of the American meteorological Society, 77, 437–471, 1996.

Kluzek, E.: CESM Research Tools: CLM4.5 in CESM1.2.0 User's Guide Documentation, http://www.cesm.ucar.edu/models/cesm1.2/clm/models/lnd/clm/doc/UsersGuide/x12544.html, 2013.

Koven, C. D., Ringeval, B., Friedlingstein, P., Ciais, P., Cadule, P., Khvorostyanov, D., Krinner, G., and Tarnocai, C.: Permafrost carbon-climate feedbacks accelerate global warming, Proceedings of the National Academy of Sciences, 108, 14 769–14 774, doi:10.1073/pnas.1103910108, 2011.

Geoscientific
Model Development
Discussions

Koven, C. D., Riley, W. J., and Stern, A.: Analysis of permafrost thermal dynamics and response to climate change in the CMIP5 Earth System Models, Journal of Climate, 26, 1877–1900, 2013.

Lawrence, D., Fisher, R., Koven, C., Oleson, K., Swenson, S., Vertenstein, M., et al.: Technical Description of version 5.0 of the Community Land Model (CLM), Tech. rep., NCAR Technical Note NCAR/TN-503+ STR, Boulder, Colorado, 2018.

5   Lawrence, D. M. and Slater, A. G.: A projection of severe near-surface permafrost degradation during the 21st century, Geophysical Research Letters, 32, doi:10.1029/2005GL025080, 2005.

Levitus, S., Antonov, J. I., Boyer, T. P., Baranova, O. K., Garcia, H. E., Locarnini, R. A., Mishonov, A. V., Reagan, J., Seidov, D., Yarosh, E. S., et al.: World ocean heat content and thermosteric sea level change (0–2000 m), 1955–2010, Geophysical Research Letters, 39, doi:10.1029/2012GL051106, 2012.

10   MacDougall, A., González-Rouco, J. F., Stevens, M. B., and Beltrami, H.: Quantification of subsurface heat storage in a GCM simulation, Geophysical Research Letters, 2008.

MacDougall, A. H. and Beltrami, H.: Impact of deforestation on subsurface temperature profiles: implications for the borehole paleoclimate record, Environmental Research Letters, 12, 074 014, doi:10.1088/1748-9326/aa7394, 2017.

MacDougall, A. H., Beltrami, H., González-Rouco, J. F., Stevens, M. B., and Bourlon, E.: Comparison of observed and General Circulation
15   Model derived continental subsurface heat flux in the Northern Hemisphere, Journal of Geophysical Research, 2010.

NCAR: Permafrost Carbon RCN forcing data, http://www.earthsystemgrid.org/dataset/ucar.cgd.ccsm4.permafrostRCN_protocol2_forcing. html, 2013.

Nicolsky, D., Romanovsky, V., Alexeev, V., and Lawrence, D.: Improved modeling of permafrost dynamics in a GCM land-surface scheme, Geophysical research letters, 34, doi:10.1029/2007GL029525, 2007.

20   O'Connor, F. M., Boucher, O., Gedney, N., Jones, C., Folberth, G., Coppell, R., Friedlingstein, P., Collins, W., Chappellaz, J., Ridley, J., et al.: Possible role of wetlands, permafrost, and methane hydrates in the methane cycle under future climate change: A review, Reviews of Geophysics, 48, 2010.

Pitman, A.: The evolution of, and revolution in, land surface schemes designed for climate models, International Journal of Climatology, 23, 479–510, doi:10.1002/joc.893, 2003.

25   Rhein, M., Rintoul, S., Aoki, S., Campos, E., Chambers, D., Feely, R. A., Gulev, S., Josey, G. C. J. S. A., Kostianoy, A., Mauritzen, C., Roemmich, D., Talley, L. D., and Wang, F.: Observations: Ocean, chap. 3, pp. 264–265, Cambridge University Press, 2013.

Riahi, K., Rao, S., Krey, V., Cho, C., Chirkov, V., Fischer, G., Kindermann, G., Nakicenovic, N., and Rafaj, P.: RCP 8.5—A scenario of comparatively high greenhouse gas emissions, Climatic Change, 109, 33, doi:10.1007/s10584-011-0149-y, 2011.

Riley, W., Subin, Z., Lawrence, D., Swenson, S., Torn, M., Meng, L., Mahowald, N., and Hess, P.: Barriers to predicting changes in global
30   terrestrial methane fluxes: analyses using CLM4Me, a methane biogeochemistry model integrated in CESM, Biogeosciences, 8, 1925–1953, doi:10.5194/bg-8-1925-2011, 2011.

Running, S. W. and Gower, S. T.: FOREST-BGC, a general model of forest ecosystem processes for regional applications. II. Dynamic carbon allocation and nitrogen budgets, Tree physiology, 9, 147–160, 1991.

Running, S. W. and Hunt, E. R.: Generalization of a forest ecosystem process model for other biomes, BIOME-BCG, and an application for
35   global-scale models, 1993.

Schmidt, G. A., Kelley, M., Nazarenko, L., Ruedy, R., and Russell, G. L.: Configuration and assessment of the GISS ModelE2 contributions to the CMIP5 archive, Journal of Advances in Modeling Earth Systems, 2014.

Schuur, E., McGuire, A., Schädel, C., Grosse, G., Harden, J., Hayes, D., Hugelius, G., Koven, C., Kuhry, P., Lawrence, D., et al.: Climate change and the permafrost carbon feedback, Nature, 520, 171–179, doi:10.1038/nature14338, 2015.

Seneviratne, S., Corti, T., Davin, E., Hirschi, M., Jaeger, E., Lehner, I., Orlowsky, B., and Teuling, A.: Investigating soil moisture-climate interactions in a changing climate: A review, Earth-Science Reviews, 2010.

5   Shangguan, W., Hengl, T., de Jesus, J. M., Yuan, H., and Dai, Y.: Mapping the global depth to bedrock for land surface modeling, Journal of Advances in Modeling Earth Systems, doi:10.1002/2016MS000686, 2017.

Slater, A. G. and Lawrence, D. M.: Diagnosing present and future permafrost from climate models, Journal of Climate, 26, 5608–5623, doi:10.1175/JCLI-D-12-00341.1, 2013.

Smerdon, J. E. and Stieglitz, M.: Simulating heat transport of harmonic temperature signals in the Earth's shallow subsurface: Lower-
10   boundary sensitivities, Geophysical research letters, 33, doi:10.1029/2006GL026816, 2006.

Stevens, M. B., Smerdon, J. E., González-Rouco, J. F., Stieglitz, M., and Beltrami, H.: Effects of bottom boundary placement on subsurface heat storage: Implications for climate model simulations, Geophysical research letters, 34, doi:10.1029/2006GL028546, 2007.

Stocker, T., Qin, D., Plattner, G. K., Tignor, M., Allen, S. K., Boschung, J., Nauels, A., Xia, Y., Bex, V., and Midgley, P. M.: Climate Change 2013: The Physical Science Basis, 2013.

15   Thomson, A. M., Calvin, K. V., Smith, S. J., Kyle, G. P., Volke, A., Patel, P., Delgado-Arias, S., Bond-Lamberty, B., Wise, M. A., Clarke, L. E., et al.: RCP4. 5: a pathway for stabilization of radiative forcing by 2100, Climatic change, 109, 77, doi:10.1007/s10584-011-0151-4, 2011.

Thornton, P. E. and Rosenbloom, N. A.: Ecosystem model spin-up: Estimating steady state conditions in a coupled terrestrial carbon and nitrogen cycle model, Ecological Modelling, 189, 25–48, doi:10.1016/j.ecolmodel.2005.04.008, 2005.

20   Thornton, P. E., Law, B. E., Gholz, H. L., Clark, K. L., Falge, E., Ellsworth, D. S., Goldstein, A., Monson, R. K., Hollinger, D., Falk, M., et al.: Modeling and measuring the effects of disturbance history and climate on carbon and water budgets in evergreen needleleaf forests, Agricultural and forest meteorology, 113, 185–222, 2002.

UCAR: Community Land Model, http://www.cesm.ucar.edu/models/clm/, 2016.

Van Vuuren, D. P., Edmonds, J., Kainuma, M., Riahi, K., Thomson, A., Hibbard, K., Hurtt, G. C., Kram, T., Krey, V., Lamarque, J.-F., et al.:
25   The representative concentration pathways: an overview, Climatic change, 109, 5, doi:10.1007/s10584-011-0148-z, 2011.

Viovy, N.: CRU-NCEPv4, CRUNCEP dataset. See http://dods. extra. cea. fr/data/p529viov/cruncep/readme. htm, 2011.

Viovy, N.: CRUNCEP Version 7 - Atmospheric Forcing Data for the Community Land Model, http://rda.ucar.edu/datasets/ds314.3/, 2018.

Wu, T., Song, L., Li, W., Wang, Z., Zhang, H., Xin, X., Zhang, Y., Zhang, L., Li, J., Wu, F., Liu, Y., Zhang, F., Shi, X., Chu, M., Zhang, J., Fang, Y., Wang, F., Lu, Y., Liu, X., Wei, M., Liu, Q., Zhou, W., Dong, M., Zhao, Q., Ji, J., Li, L., and Zhou, M.: An Overview of BCC
30   Climate System Model Development and Application for Climate Change Studies, Journal of Meteorological Research, 2014.